

University of Alberta

Electron Acceleration by Inertial Alfvén Waves

by

José Mauricio Blanco-Benavides

A thesis submitted to the Faculty of Graduate Studies and Research in partial
fulfilment of the requirements for the degree of

Master of Science

Department of Physics

©José Mauricio Blanco-Benavides

Spring 2011

Edmonton, Alberta

Permission is hereby granted to the University of Alberta Libraries to reproduce single copies of this thesis and to lend or sell such copies for private, scholarly or scientific research purposes only. Where the thesis is converted to, or otherwise made available in digital form, the University of Alberta will advise potential users of the thesis of these terms.

The author reserves all other publication and other rights in association with the copyright in the thesis and, except as herein before provided, neither the thesis nor any substantial portion thereof may be printed or otherwise reproduced in any material form whatsoever without the author's prior written permission.

To

Life, and whomever made it

Abstract

The nightside auroral region is known to be the most powerful source of radiation from Earth to space. Emitted radiation reaches up to 10^9 watt, with frequencies ranging 100 - 600 kHz, and is known as Auroral Kilometric radiation (AKR) *Parks* [2004].

AKR is generated through coherent emission by highly energetic electrons. In order to understand how these electrons are energized, a 1D test particle code has been written to study wave-particle interactions at the inertial regime. The computational model reproduces particle dynamics and wave properties in uniform and non-uniform conditions of magnetic field and plasma density. Simulations of wave-particle interactions have also been performed and resulting observations were compared with similar publications. The model is intended to be used to obtain unstable particle distributions that are characteristic of the auroral region, and will be utilized in future studies of generation mechanisms of AKR.

Acknowledgements

I owe a huge acknowledgement to my supervisor, Dr. Robert Rankin, who had to put up with me with infinite patience for my lack of meaningful results during most of the realization of this work, and despite everything provided also with constant academic and logistic support.

A big thanks also to Dr. Clare Watt, without whom i would be for sure still struggling on one of the many times i run out of ideas. Every single discussion we had translated into a considerable improvement, and in not too few cases, total salvation of this work.

Table of Contents

1	Introduction	1
1.1	Magnetospheric Structure	3
1.1.1	Magnetic and plasma convection	4
1.1.2	Magnetosphere-Ionosphere coupling	6
1.2	Auroral Kilometric Radiation	7
1.2.1	Source Region	8
1.2.2	Theory of AKR generation by nonthermal distributions	9
1.2.3	Electron Cyclotron Maser	10
1.2.4	Electron Cyclotron Maser Instability	13
1.3	Alfvén waves as potential sources of AKR	17
1.3.1	MHD waves	18
1.3.2	Dispersive Alfvén Waves (DAW)	22
2	Test Particle and Wave Algorithms	26
2.1	Basic particle motion in externally applied fields	29
2.1.1	Motion due to a constant electric field	30
2.1.2	Motion due to a constant magnetic field	30
2.1.3	More complicated particle drifts	31
2.1.4	Magnetic moment and flux conservation	33
2.2	Wave propagation	34
2.3	Numerical Algorithm	36
2.3.1	Wave discretization	37
2.3.2	Wave Dispersion Analysis	38
2.3.3	Electric field interpolation	39
2.3.4	Background Plasma and Magnetic Field	40
2.3.5	Background Magnetic Field	41
2.3.6	Test particle dynamics	42
2.4	Scaling of physical quantities	45
3	Code tests	47
3.1	Test 1: Dynamics of a single particle	47
3.1.1	Obtained results	48
3.2	Test 2: Wave propagation in a uniform medium	50
3.3	Test 3: Wave propagation on a nonuniform medium	51

TABLE OF CONTENTS

3.3.1	Expected behaviour	51
3.3.2	Simulation output	52
3.4	Test 4: Wave - particle interaction in homogeneous medium	54
4	Results	57
4.1	Background plasma properties	57
4.2	Consistency of the equilibrium distribution	58
4.2.1	Determination of the electrostatic potential	60
4.3	Building up the equilibrium distribution	61
4.4	Wave-plasma interaction at an inhomogeneous media	66
4.4.1	Looking for unstable distributions	70
5	Conclusion	73
	Bibliography	75

List of Tables

2.1	Averages and rms predictions for a maxwellian distribution	44
2.2	Scaling factors for physical quantities	46
3.1	Expected (τ_E) and Numerical (τ_N) bounce periods in seconds, after the first bounce, at several pitch angles and energies for one particle.	49
3.2	Expected (E) and first reached Numerical (N) turning points for a particle with energy 1000 eV at several pitch angles.	50
3.3	Constant numerical parameters used in all simulations	51
3.4	Expected ($V_{\parallel E}$) and Numerical ($V_{\parallel N}$) phase velocities for different β parameters	52
3.5	Numerical parameters for a simulation of IAW propagation into a Maxwellian plasma in a uniform magnetic field	54
4.1	Numerical parameters defining background magnetic field and plasma density	63
4.2	Several typical velocities of the initial distribution of loaded particles with temperature $T = 10$ eV	65
4.3	Numerical parameters for an IAW pulse into an inhomogeneous magnetic field	66

List of Figures

1.1	Magnetospheric structure (<i>taken from http://www-ssc.igpp.ucla.edu/ssc/tutorial/magnetosphere.html</i>)	5
1.2	Resonance curve for (a) nonrelativistic and (b) semirelativistic interaction.	10
1.3	Effective phase diagram. Particles for which $\mathbf{E} \cdot \mathbf{v} < 0$ (shaded area) are energy gaining particles, and particles located in the first and fourth quadrant are energy losing particles. (a) azimuthal bunching, (b) axial bunching (<i>Modified from Chu [2004]</i>)	12
1.4	Dispersion diagrams for a distribution described by equation (1.20). (a) and (b) are solutions for the relativistic case, (c) and (d) are solutions of the nonrelativistic case, for $\gamma_0 = 1.2$ and $\omega_{ce}/(\gamma_0\omega_{pe}) = 10$ (<i>After Chu [2004]</i>)	14
1.5	Loss cone distribution. The dotted ellipses represent the resonance curve harmonics. (<i>After Su et al. [2007]</i>)	15
1.6	Shell distribution and its resonance curve (<i>After Su et al. [2007]</i>)	16
2.1	Discretization scheme. Scalar and vector potentials are leap-frogged in space (and time). The electric field is at every iteration calculated in the same locations at which the vector potential is defined.	37
2.2	Diagram representing the update procedure into the program. Wave equations are updated one from the other. Once updated, the electric field and particle movement are calculated. A single iteration requires the calculation of a few possible trajectories, from which the final approximation is obtained.	43
3.1	Phase space and temporal behaviour for a particle embedded in a quadratic magnetic field.	49
3.2	Waveform for propagation in homogeneous media at different times.	51
3.3	Snapshots of wave propagation into an inhomogeneous medium. Alfvén velocity profile is also shown	53
3.4	<i>left</i> A representation of parallel velocity density and <i>right</i> parallel electric field along the spatial domain (position along domain is represented by the vertical axis)	56

LIST OF FIGURES

4.1	Variation of density, electrostatic potential and temperature along a section of magnetic field line. The parameters given are: $n_{H_2} = 10 \text{ cm}^{-3}$, $n_{O_2} = 2 \times 10^5 \text{ cm}^{-3}$, $T_c = 10 \text{ eV}$, $T_w = 1 \text{ keV}$, $s_i = 4.5R_e$ and $h_0 = .2R_e$	62
4.2	Background plasma properties	62
4.3	Ion density as a function of position. Initial plasma is distributed spatially in the interval $[0, 3.5R_e]$	64
4.4	Local $(v_{\parallel}, v_{\perp})$ electron density at few different places of the simulation domain	64
4.5	Time evolution of electron density as a function of position. (<i>left</i>) No new particles are introduced. (<i>right</i>) New particles are injected through boundaries at every time step.	67
4.6	Time evolution of electron density in phase. (<i>left</i>) No new particles are introduced. (<i>right</i>) New particles are injected through boundaries at every time step.	68
4.7	Wave propagation into an inhomogeneous magnetic field. The vertical axis represents distance along the magnetic field line $L = 4$, starting at the equator and going towards the ionosphere at higher latitudes. (<i>left</i>) Distributions of parallel velocities. Relative densities are constrained to values between 0 and 250. (<i>right</i>) Wave parallel electric field.	69
4.8	Local $(v_{\parallel}, v_{\perp})$ electron density at approximately $1.75 R_e$ at $t = 0.6 \text{ s}$	72

Chapter 1

Introduction

Each plasma-related phenomena that occurs naturally above Earth's atmosphere is ultimately driven by solar activity. In fact, the two regions that constitute the boundary between the atmosphere and outer space, namely the ionosphere and magnetosphere, correspond to plasma regimes coexisting permanently thanks to solar energy. Their properties, however, are of a completely different nature; the magnetosphere is populated by a low density, relatively warm and fully ionized plasma, mostly composed of particles of solar origin that are expelled in the process of coronal expansion and eventually trapped into Earth's magnetic field. In the macroscopic picture, at length scales close to $\sim R_e$, the absence of collisions allows magnetospheric particles to move freely along magnetic field lines, while simultaneously drifting around Earth depending on their energy. Such azimuthal motion is important in forming the ring current, but at auroral latitudes the current of particles perpendicular to the geomagnetic field is rather small, and can be considered negligible. At the Ionosphere, solar UV radiation ionizes a fraction of the high-density constituent of molecules at the top of the atmosphere. The high density of neutrals in the ionosphere implies an environment where collisions happen frequently; the conductivity becomes finite and currents develop perpendicular to the background magnetic field. Collisions involving ions dominate due to their high cross section, and perpendicularly deflected ions form so-called *Pedersen currents*. The currents resulting from the absence of deflected ions, now forming the Pedersen currents, from their original trajectories are known as *Hall currents*. Both Pedersen and Hall currents allow fluxes of particles (currents) transverse to the geomagnetic field, and these are ultimately connected with field-aligned current systems flowing into and out of the magnetosphere.

Although the atmosphere, ionosphere and magnetosphere are adjacent one to

another, there are no definite boundaries between them. As altitude increases, the gas density in the ionosphere decreases and collisions become gradually less frequent. The rate of recombination also decreases so that the ionosphere slowly merges with the magnetosphere. The current systems naturally change from being largely perpendicular at low altitude to mostly field-aligned at high altitude. The transition just described is rather more complicated at polar latitudes, where geomagnetic field lines change from being closed to open. The boundary between open and closed magnetic field lines provides favourable conditions for direct mass and energy transport between the magnetosphere and the solar wind. As part of the complex processes that take part in the coupling, magnetic field-aligned currents generated at the equatorial region due to plasma convection [[Vogt, 2002](#)] are driven along magnetic field lines and closed by perpendicular currents in the ionosphere. In times of quiet activity, the thermal energy of the plasma is enough to carry the field-aligned currents, but in active times these currents lead to the establishment of magnetic field-aligned electric fields that produce Earthward electron acceleration and anti-Earthward ion acceleration [[Paschmann et al., 2003](#)]. These electric fields have been proven to exist through analysis of spacecraft data [[Louarn et al., 1990](#)]. The presence of electric fields parallel to the background magnetic field in the auroral transition region is an essential feature of the AKR (Auroral Kilometric Radiation) source region [[Treumann, 2006](#)]. Together with the converging nature of the magnetic field, parallel electric fields cause a depletion region of low energy particles known as the *Auroral Cavity*. By the action of such fields, unstable particle distributions develop, providing a free source of energy that can be used in the amplification of coherent radio emission associated with AKR.

The general magnetospheric convection cycle attributed to processes mentioned above provides only one mechanism for the existence of parallel electric fields in the Auroral Cavity. Transient perturbations in the magnetospheric environment very often launch dispersive shear Alfvén waves (DAWs) as a response. These waves move along magnetic field lines down to the ionosphere, where electron inertial effects become important as the waves transition into cold ionospheric plasma. DAWs are capable of producing electron acceleration through the generation of parallel electric fields. They are further classified as Kinetic Alfvén Waves (KAWs) and as Inertial Alfvén Waves (IAWs); the KAW regime is associated with warm plasma (field-aligned electric fields in KAWs are dominated by electron pressure effects), while IAWs are found in cold plasmas where electron inertia drives the parallel electric field.

This thesis seeks to contribute to the understanding of electron acceleration

produced by IAWs. The methodology involves using a one-dimensional test particle algorithm and the model for wave propagation described in *Stasiewicz et al. [2000]* and *Thompson and Lysak [1996]*. The model plasma region considered consists of a mirror field that is assumed to be filled with a Maxwellian plasma that is led to interact with a prescribed IAW pulse. Numerical approximations are used to calculate the fields of the IAWs at the position of every particle. In particular, a 4th-order Runge-Kutta integration scheme is used to estimate the temporal evolution of the trajectories of particles using electric and magnetic forces as input. The computer algorithm and magnetic field configuration is intended to allow unstable particle distributions to form that may in turn be associated with generation of AKR. The scope of the thesis is to determine plasma and IAW conditions that are favourable for generation of AKR, but not to provide detailed analysis of the AKR process. This is left for future study.

The thesis contains five chapters. In chapter 1, the main regions of the magnetospheric environment are described, including the magnetospheric-ionospheric coupling region, which contains the AKR source region. The context in which IAWs propagate from the magnetosphere to the ionosphere is described, including the conditions under which modes with finite perpendicular wavenumber k_{\perp} develop, and how they can accelerate particles.

Chapter 2 deals with a complete description of the computational algorithms that are used. In chapter 3, various tests of the algorithms are described. Chapter 4 presents results of simulations and in chapter 5 some conclusions and suggestions for future work are given.

1.1 Magnetospheric Structure

At the surface of the Sun, high temperatures ($\sim 10^6$ K) maintain ionized Hydrogen. In this region, approximately 1/2 of the electrons that are present have sufficient thermal energy to overcome the solar gravity force and escape to space, while less than 1% of the ions do [*Parks, 2004*]. This charge imbalance produces large electric fields that accelerate ions outward. As a result, a magnetized, supersonic (~ 500 km/s) plasma known as the *Solar Wind* is continuously released from the solar atmosphere. Close to Earth, the composition of the Solar Wind is almost exclusively H^+ , He^{++} ($\sim 4\%$), and traces of heavier ions, with density ~ 7 cm $^{-3}$ and temperatures $T_i \sim T_e \sim 10$ eV. The solar wind plasma is coupled to an interplanetary magnetic field of the order of 10 nT [*Paschmann et al., 2003*].

The interaction of the solar wind with planet Earth involves the geomagnetic

field. For practical purposes, close to Earth the magnetic field in its unperturbed form is accurately approximated as a dipole field, with the dipole axis rotated 12° from the rotational axis. The extent and shape of Earth's magnetic field is, however, determined by a balance between the magnetic pressure of the dipolar field and the magnetic stresses and momentum flux associated with the Solar Wind. Earth's magnetic field obstructs the free transit of Solar Wind particles, deflecting them around Earth rather than allowing them to impinge directly on the atmosphere. The spatial region inside of which the magnetic field of Earth stands off the free expansion of the solar wind is what we know as the *Magnetosphere*.

From the point of view of the reference frame of the Solar Wind, Earth travels into the solar wind with supersonic velocity, creating a *Bow Shock* in front of it; at the Bow Shock, Solar Wind particles are slowed to subsonic velocities with respect to the Earth frame, losing most of their kinetic energy into heat [*Kivelson and Russell, 1995*]. The region between the Bow Shock and the actual Magnetosphere is called the *Magnetosheath*, a region populated with denser, thermalized solar wind particles.

Figure 1.1 shows the typical configuration of the magnetospheric system, where solar plasma is advected from the left towards Earth. The momentum associated with the stream of solar wind particles forces the magnetospheric field to compress on the dayside, moving magnetic field lines closer together. On the nightside, on the other hand, Earth's magnetic field expands antisunward into a *Magnetotail* by the action of lateral stresses of the streaming Solar Wind. Inside the Magnetotail, there are several regions with different plasma properties, defined by their density and magnetic topology. The detailed structure of the magnetotail also corresponds to the magnetic convection "Dungey" cycle driven by continuous streaming of the Solar Wind.

1.1.1 Magnetic and plasma convection

The interplanetary magnetic field (IMF) and Solar Wind plasma are not able to directly penetrate the Magnetosphere. Instead, magnetic field lines drape over the Magnetosphere and most of the Magnetosheath plasma is forced to surround Earth. This causes the geomagnetic field to resemble a teardrop, which acts as a shield to the solar wind. As magnetosheath plasma is dragged along the Magnetopause, it produces tangential stresses that transfer momentum to magnetospheric plasma, causing it to move tailward.

At the nose of the Magnetosphere, flow velocities are low enough as to make

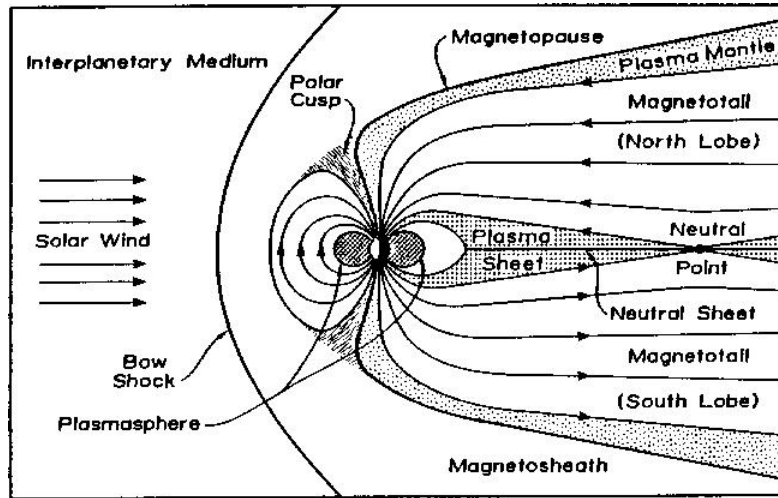


Figure 1.1: Magnetospheric structure (taken from <http://www-ssc.igpp.ucla.edu/ssc/tutorial/magnetosphere.html>)

diffusion effects important. When diffusion takes place under southward IMF conditions, magnetic field lines on either side of the Magnetopause will break and reconnect into two open magnetic lines starting one at each pole and extending into open space. At the diffusion zone, the magnetohydrodynamic approximation is no longer valid, allowing plasma to diffuse across flux tubes, thus enabling mass interchange between the Magnetosheath and the Magnetosphere. Reconnected field lines are forced to move antisunward, carrying their flux tube plasma with them. High latitude open magnetic field lines fill the *Plasma Mantle* with hot plasma of solar origin. As they are dragged antisunward they move to lower latitudes into the *Tail lobes*, where by that time they have substituted some of their hot plasma with cold plasma of ionospheric origin [Kivelson and Russell, 1995], [www.meter.ucar.edu]. Eventually, in the distant magnetotail, these open magnetic field lines will converge and reconnect again into one magnetic line that will couple to the Solar Wind, and one closed geomagnetic field line that is convected earthward. Geomagnetic field lines produced by tail reconnection are pushed earthwards into the *Plasma Sheet Boundary Layer* (PSBL), moving away from the reconnection point by means of the magnetic pressure exerted by other open magnetic field lines dragged to the reconnection point. At the PSBL, plasma beams move along and against the magnetic field as a consequence of reconnection and magnetic mirror forces at auroral latitudes, respectively [Kivelson and Russell, 1995]. Closer to Earth is the *Plasma Sheet*, populated by a denser ($\sim 0.1 - 1 \text{ cm}^{-3}$), hotter ($T_i = 2 -$

20 keV, $T_e \sim 0.4 - 4$ keV) and slower plasma originated from the thermalization of the Plasma Sheet Boundary Layer. Both the PS and PSBL map to the ionosphere through the nightside auroral region. At the inner region of the Plasma Sheet lie the *Plasmasphere* and the *Radiation Belts*. The Plasma Sheet-Plasmasphere border is characterized by a large increase in density and large decrease in temperature. The Radiation Belts are constituted by a trapped population of high energetic particles (> 1 MeV), with their motion constrained by the three adiabatic invariants: the magnetic moment, the bounce motion between the magnetic poles, and the flux invariant [*Paschmann et al.*, 2003].

1.1.2 Magnetosphere-Ionosphere coupling

The magnetosphere-ionosphere transition region is the most important in terms of the AKR phenomena. Although the vertical extension of the ionosphere spans roughly $\sim 90 - \sim 300$ km over the surface of the Earth (small compared with typical length scales of the Magnetosphere $\sim R_e$), effects of its coupling with the magnetosphere extend over several 1000 km altitude.

In the magnetosphere, the scarcity of neutral particles guarantees a practically perfect conducting medium. The light electrons move freely along the magnetic field, screening any electric fields that may arise. In a reference frame moving with the plasma bulk velocity, at scales larger than the Debye length, the electric field is always zero. However, when moving to a reference frame stationary with respect to Earth, a perpendicular convection electric field $\mathbf{E} + \mathbf{v} \times \mathbf{B} = 0$ results. From this point of view, the plasma moves freely along the magnetic field and drifts with the perpendicular electric field; none of these particular processes involving the generation of currents perpendicular to the magnetic field.

At the ionosphere, there is a high density of neutral molecules. Collisions of ions and electrons with neutral particles interrupt the free motion along magnetic field lines and the $\mathbf{E} \times \mathbf{B}$ drift, thereby reducing the conductivity to some finite value that depends on the density of neutrals. For an ionospheric plasma that drifts perpendicular to the convection electric field, ion-neutral collisions cause the ions to drift along the electric field, thus generating two perpendicular current systems; a *Pedersen current* directed along the electric field, and a *Hall current* which is opposite to the electron drift velocity. For a system that is nearly electrostatic, the magnetospheric convection electric field is mapped along magnetic field lines into the ionosphere, where currents can flow perpendicularly to the magnetic field.

The magnetospheric environment also supports more transient phenomena such

as Alfvén waves. These Alfvén waves are very efficient at transporting wave and plasma energy throughout the magnetosphere. At small scales they manifest as dispersive Alfvén waves (DAWs), which accelerate particles and drive Pedersen currents in the ionosphere.

1.2 Auroral Kilometric Radiation

The first spacecraft equipped with radio detectors discovered that Earth can act as a powerful radio emitter. The most intense radiation covers the 100 - 600 kHz range. Since radiation at 300 kHz corresponds to a wavelength of 1 km, this radiation was given the name of Auroral Kilometric Radiation (AKR). The emitted power ranges to about 10^7 W during small substorms and 10^9 W during strong substorms. The rate of thermal to AKR radiation conversion is estimated to be $\sim 0.1 - 1\%$, which is considered very high [Paschmann *et al.*, 2003]. Brightness temperatures can reach up to 10^{20} K [Ergun *et al.*, 2000], suggesting a coherent emission mechanism instead of a thermal one, since no sources of such high temperatures are found in the planet. Radiation propagates primarily in the RX mode, although LO and Z modes are often present in lower levels (for a detailed description of these emissions, see Kivelson and Russell [1995]). The AKR spectrum is discrete and narrowband, consisting of intense emission events composed out of the superposition of many narrow-band structures with bandwidths of ~ 1 kHz and lifetimes of < 1 s [Paschmann *et al.*, 2003] [Treumann, 2006].

Generation of AKR is provided by amplification of waves after resonant interaction with the gyration motion of nonthermal electron distributions, as described by the following resonance condition

$$\omega - k_{\parallel}v_{\parallel} - s\frac{\omega_{ce}}{\gamma} = 0 \quad (1.1)$$

Here, ω_{ce} is the particle cyclotron frequency, s represents the cyclotron harmonic number, γ is the relativistic factor, v_{\parallel} is the particle velocity parallel to the magnetic field, and (k_{\parallel}, ω) are the parameters of the amplified wave.

High efficiency in wave amplification is possible when there is an absence of dissipation mechanisms, such as heating and viscosity. In such cases, an energized plasma will store its excess energy in the particle distribution, where it is available to feed wave instabilities [Treumann, 2006]. The existence of a nonthermal distribution relies on special conditions at the source region, the first of them being the absence of collisions already provided by the magnetospheric environment.

1.2.1 Source Region

In the high altitude auroral ionosphere, located approximately between 1000 - 8000 km towards the nightside, at about $70^\circ \pm 3^\circ$ latitude, the converging magnetic field and the presence of an upward electric field work together to maintain unstable particle distributions. Along the magnetic field, the mirror force acts to decelerate the incoming magnetospheric plasma. At the same time, the electric field accelerates ions upwards and electrons downwards, generating relatively strong currents, and preventing the advection of cold electrons from the ionosphere. The magnetic mirror and electric forces are opposite for electrons, and compete for electrons moving upwards and downwards, respectively. Incoming magnetospheric electrons with low parallel velocities are more likely to be rejected back by the mirror force. Particles within the loss cone get filtered in this manner and precipitate into the atmosphere, while others initially not inside the loss cone are included into it due to the parallel acceleration. As a result, there is a depletion of low energy particles ($< 1 \text{ cm}^{-3}$ [Pritchett, 1984]) commonly referred to as *the Auroral Plasma Cavity*.

Spacecrafts Viking [Louarn *et al.*, 1990], Freja [Louarn *et al.*, 1994] and FAST [Ergun *et al.*, 1998] [Ergun *et al.*, 2000] have performed trajectories across the Auroral Cavity and confirmed the existence of upward electric fields and a low density cavity nearly depleted of cold plasma. Further features of the source region already confirmed by *in situ* measurements were summarized by Treumann [2006] and include: field aligned upward currents, ion and electron fluxes with average energies of 10 keV, strong RX mode radiation at frequencies $\omega < \omega_{ce}$, circularly polarized radiation emitted perpendicularly to the ambient magnetic field, and unstable electron distributions.

As mentioned previously, there is observational evidence indicating that AKR that is collocated with the auroral region is the result of many elemental radiators, also known as *electron holes*, each of them showing short bandwidth ($< 1 \text{ kHz}$) and moving at velocities of the order of a few thousands km/s [Treumann, 2006]. Measurements of the modulation in a single of these elemental radiators indicate that these are very small structures of the order of the Debye length [Treumann, 2006].

1.2.2 Theory of AKR generation by nonthermal distributions

The resonant condition (1.1), when relativistic considerations are taken into consideration, describes an ellipse in phase space

$$\left(\frac{v_{\parallel}/c - v_{\parallel 0}/c}{a}\right)^2 + \left(\frac{v_{\perp}/c}{b}\right)^2 = 1 \quad (1.2)$$

with the ellipse centered on the parallel velocity axis

$$\frac{v_{\parallel 0}}{c} = \frac{\omega kc}{\alpha^2} \quad (1.3)$$

where $\alpha^2 = (s\omega_{ce})^2 + (kc)^2$. The intersections of the ellipse with the phase space axes are defined by

$$a^2 = \frac{(s\omega_{ce})^2 (\alpha^2 - \omega^2)}{\alpha^4} \quad (1.4)$$

$$b^2 = \frac{\alpha^2 - \omega^2}{\alpha^2} \quad (1.5)$$

The position and shape of the resonant curve depends entirely on ω , s , ω_{ce} and k_{\parallel} . Inspection of the resonant condition reveals that the nonrelativistic case ($\gamma \simeq 1$ in equation (1.1)) reduces the ellipse to a straight line.

$$v_{\parallel nr} = \frac{s\omega_{ce} - \omega}{k_{\parallel}} \quad (1.6)$$

If there is a positive slope in the electron distribution in the vicinity of the resonant velocity, it is possible for wave amplification to take place. This is the potential source of AKR. The dispersion relation for this process relates the wave growth rate with the integral along the phase space of an expression that includes the gradient of the distribution in the numerator and the resonance condition in the denominator. Positive gradient of the distribution contributes to wave emission, while negative gradients add to absorption of radiation. Since each particle is weighted by the amount $(\omega - k_{\parallel}v_{\parallel} - s\omega_{ce}/\gamma)^{-1}$, then contributions from particles in resonance are amplified with respect to the rest of the distribution; the integral over the whole space phase can be approximated as the integral along the curve of resonance [Melrose and Dulk, 1982]. The specific condition for wave growth depend on the gradient of the distribution function with respect to the momentum

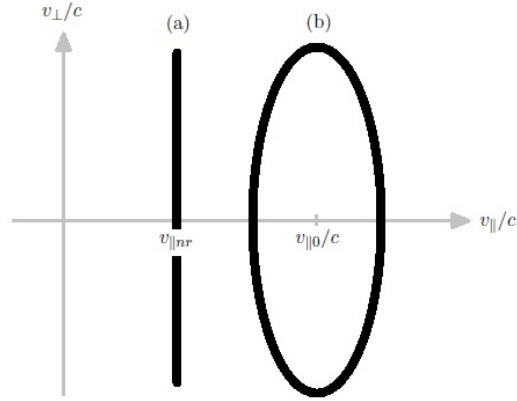


Figure 1.2: Resonance curve for (a) nonrelativistic and (b) semirelativistic interaction.

components p_{\parallel} and p_{\perp} [Melrose, 2009]

$$\left[\frac{s\omega_{ce}}{v_{\perp}} \frac{\partial}{\partial p_{\perp}} + k_{\parallel} \frac{\partial}{\partial p_{\parallel}} \right] f(p_{\perp}, p_{\parallel}) > 0 \quad (1.7)$$

Physically, for a given electron distribution and background magnetic field, from all the wave modes present the one to be amplified is the one for which its resonant ellipse fits more closely the regions in phase space where the distribution function has a growing trend. In other words, amplification of the wave relies on the wave being in resonance with the most number of energetic particles possible. The subsections below summarize the potential types of unstable electron distributions that act as possible sources of AKR.

1.2.3 Electron Cyclotron Maser

Emission/Absorption by a single electron

Consider a relativistic electron embedded in a homogeneous magnetic field $\mathbf{B}_0 = |B_0|\hat{\mathbf{z}}$, and influenced by an electromagnetic wave propagating along $\hat{\mathbf{z}}$, which, at the position of the particle, is described by

$$\mathbf{E}_{\perp}(z, t) = E_{\perp} (\cos(\omega t - k_{\parallel}z)\hat{\mathbf{x}} + \sin(\omega t - k_{\parallel}z)\hat{\mathbf{y}}) \quad (1.8)$$

$$\mathbf{B}_\perp(z, t) = \frac{E_\perp}{\omega/k_\parallel} (-\sin(\omega t - k_\parallel z)\hat{\mathbf{x}} + \cos(\omega t - k_\parallel z)\hat{\mathbf{y}}) \quad (1.9)$$

For a given initial orientation θ of the particle with respect to the $\hat{\mathbf{x}}$ axis, the angle in velocity space is $\phi = \theta + \pi/2$, which is typical of circular motion. Since both the electric and magnetic field perturbations tend to drive the gyrocenter out of its initial trajectory, it is convenient to use ϕ to calculate the angular velocity. For relatively weak fields, the phase change is very close to the relativistic cyclotron frequency $\dot{\phi} \simeq \omega_{ce}/\gamma$.

Regarding the particle, its velocity is

$$\mathbf{v} = v_\perp (\cos \phi \hat{\mathbf{x}} + \sin \phi \hat{\mathbf{y}}) + v_\parallel \hat{\mathbf{z}} \quad (1.10)$$

A positive (negative) change in energy denotes absorption (emission) of radiation. The variation of energy is given by the work done during an infinitesimal displacement of the electron.

$$\begin{aligned} m_e c^2 \frac{d}{dt}(\gamma - 1) &= \frac{d}{dt} [(-e(\mathbf{E} + \mathbf{v} \times \mathbf{B})) \cdot d\mathbf{r}] \\ &= -e\mathbf{E} \cdot \mathbf{v} \\ &= -eE_0 v_\perp \cos(\omega t - k_\parallel z - \phi) \end{aligned} \quad (1.11)$$

Phase drifts

Equation (1.11) defines regions of energy gain ($\mathbf{v}_\perp \cdot \mathbf{E}_\perp < 0$) and energy loss ($\mathbf{v}_\perp \cdot \mathbf{E}_\perp > 0$). In a reference frame rotating with frequency ω around the vertical axis and located at $z = 0$, the gaining region includes the second and third quadrants of its xy -plane, while the first and fourth quadrants constitute the losing energy region. In this system, a particles *effective* phase has a value of

$$\phi_{eff} = k_\parallel z + \phi \quad (1.12)$$

which changes in time as

$$\frac{d\phi_{eff}}{dt} \simeq k_\parallel v_z + \frac{\omega_{ce}}{\gamma} \quad (1.13)$$

Consider the relativistic effect on the phase variation (1.13). According to the LHS in equation (1.11), the value of the relativistic factor γ increases if the particle lies in the gaining region, which means that the rotation rate ω_{ce}/γ decreases, lead-

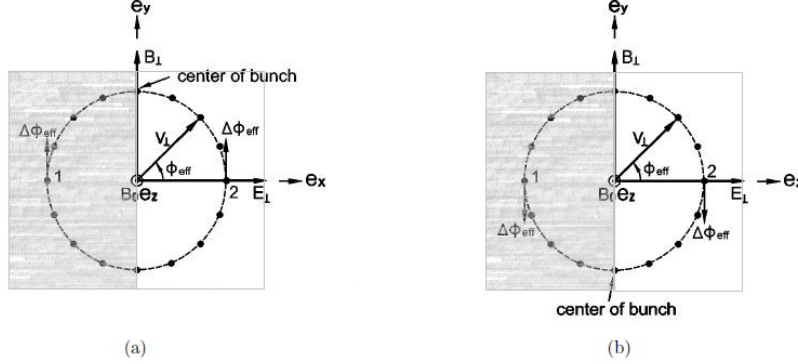


Figure 1.3: Effective phase diagram. Particles for which $\mathbf{E} \cdot \mathbf{v} < 0$ (shaded area) are energy gaining particles, and particles located in the first and fourth quadrant are energy losing particles. (a) azimuthal bunching, (b) axial bunching (*Modified from Chu [2004]*)

ing to a $\Delta\phi_{eff} < 0$. Using the same logic, at the losing energy region, the quantity ω_{ce}/γ increases due to the reduction of the relativistic mass, which produces an advance in phase $\Delta\phi_{eff} > 0$. In both cases, electrons tend to bunch to $\phi_{eff} = \pi/2$.

So far, the *coherent* nature of the radiation has not been introduced. Such an effect appears when the cyclotron frequency is different from the wave frequency. Independently of any of the bunching processes, electrons tend to rotate at the cyclotron frequency. If $\omega_{ce,eff} < \omega$, the electrons (including the bunched ones) rotate coherently in the clockwise sense. As the center of the bunch is dragged along into the gaining region, all bunched particles contribute to wave amplification. If $\omega_{ce,eff} > \omega$, bunched particles move to the losing energy region, producing coherent absorption.

Acceleration in the axial direction produced by the wave magnetic field also affects the phase; at the first and fourth quadrants, $-\hat{\mathbf{v}}_{\perp} \times \hat{\mathbf{B}}_{\perp} = -\hat{\mathbf{z}}$, and consequently, the axial velocity decreases. After one period $k_{\parallel}z$ will have a lesser value. At the region spanned by the second and third quadrants, the magnetic force points in the opposite direction ($\hat{\mathbf{z}}$), so an increase in $k_{\parallel}z$ is expected. Both cases drive the electrons to $\phi_{eff} = 3\pi/2$. Again, coherent radiation results from a detuned cyclotron frequency. In this case, however, $\omega_{ce,eff} > \omega$ produce emission, while $\omega_{ce,eff} < \omega$ induce absorption.

Both azimuthal and axial bunching have opposite effects on the electrons; the amount and kind of radiation taking place will depend on the relativistic or non-

relativistic nature of the interaction. Azimuthal bunching will take place in high frequency waves, since these waves are the ones capable of resonate with relativistic electrons. Axial bunching, on the other hand, dominates if electrons resonate with low frequency waves.

1.2.4 Electron Cyclotron Maser Instability

Any process of amplification of waves from the free energy of the local plasma distribution is technically an instability, and therefore, can be analyzed using plasma kinetic theory. Let us picture a plasma where high energy electrons in the presence of a uniform magnetic field $\mathbf{B}_0 = B_0 \hat{\mathbf{z}}$ interact with a small amplitude circular perturbation of the form

$$\delta \mathbf{E} = E_0 (\hat{\mathbf{x}} + i \hat{\mathbf{y}}) e^{i(kz - \omega t)} \quad (1.14)$$

$$\delta \mathbf{B} = \frac{kc}{\omega} \hat{\mathbf{z}} \times \delta \mathbf{E} \quad (1.15)$$

In the case of high frequency waves, the ions are approximately immobile. To first order, the Vlasov equation reads [Chu, 2004][Treumann, 2006]

$$\frac{\partial \delta f}{\partial t} + \mathbf{v} \cdot \nabla \delta f - e \mathbf{v} \times \mathbf{B}_0 \cdot \nabla_{\mathbf{p}} \delta f - e (\delta \mathbf{E} + \mathbf{v} \times \delta \mathbf{B}) \cdot \nabla_{\mathbf{p}} f_0 = 0 \quad (1.16)$$

where $\mathbf{p} = m_e \gamma \mathbf{v}$ represents the relativistic momentum. The field equation in terms of Faraday and Ampere laws is defined by

$$\nabla \times \nabla \times \delta \mathbf{E} = -\frac{1}{c^2} \frac{\partial^2 \delta \mathbf{E}}{\partial t^2} - \frac{\partial \mathbf{j}}{\partial t} \quad (1.17)$$

where the perturbed current is carried by the mobile electrons:

$$\mathbf{j} = -e \int d^3 p \mathbf{v} \delta f \quad (1.18)$$

The dispersion relation depends on the unperturbed distribution and is given by [Chu, 2004]

$$\omega^2 - (kc)^2 = -\pi \omega_{pe} \int_0^\infty dp_\perp p_\perp \int_{-\infty}^\infty dp_\parallel \frac{\left(\omega - \frac{kp_\parallel}{\gamma m_e} \right) p_\perp \frac{\partial f_0}{\partial p_\perp} + \frac{k}{\gamma m_e} p_\perp^2 \frac{\partial f_0}{\partial p_\parallel}}{\gamma \omega - \frac{kp_\parallel}{m_e} - \omega_{ce}} \quad (1.19)$$

with $\omega_{pe} = n_0 e^2 / (m_e \epsilon_0)$, $\omega_{ce} = eB_0 / m_e$ and $\gamma = \sqrt{1 + p^2 / (m_e c)^2}$.

A uniform magnetic field favours a distribution of gyrating particles, and if it is assumed that all particles have the same energy and just gyrate in the plane perpendicular to $\hat{\mathbf{z}}$, the zero-order distribution is

$$f_0(p) = \frac{\delta(p_\perp - p_{\perp 0})\delta(p_\parallel)}{2\pi p_\perp} \quad (1.20)$$

with solution to the dispersion equation

$$\omega^2 - (kc)^2 = \frac{\omega_{pe}^2}{\gamma_0} \left[\frac{\omega}{\omega - \omega_{ce}/\gamma_0} + \frac{v_{\perp 0}^2 (k^2 c^2 - \omega^2)}{2c^2 (\omega - \omega_{ce}/\gamma_0)^2} \right] \quad (1.21)$$

The nonrelativistic dispersion was also reported in [Chu \[2004\]](#) for comparison purposes

$$\omega^2 - (kc)^2 = \omega_{pe}^2 \left[\frac{\omega}{\omega - \omega_{ce}} + \frac{v_{\perp 0}^2 k^2}{2(\omega - \omega_{ce})^2} \right] \quad (1.22)$$

Both solutions are shown in figure 1.4. These are identified as fast ($\omega/k_\parallel > c$) and slow ($\omega/k_\parallel < c$) modes. The diagram shows that both modes can be driven unstable in the relativistic case, but only the slow mode shows up in the nonrelativistic case. Then the slow mode is identified as of nonrelativistic origin (axial bunching), and the fast mode as of relativistic origin (azimuthal bunching).

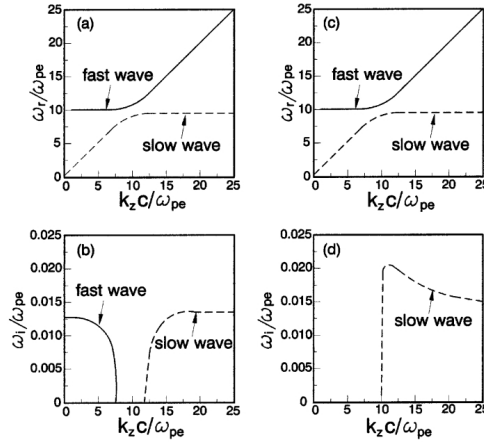


Figure 1.4: Dispersion diagrams for a distribution described by equation (1.20). (a) and (b) are solutions for the relativistic case, (c) and (d) are solutions of the nonrelativistic case, for $\gamma_0 = 1.2$ and $\omega_{ce}/(\gamma_0 \omega_{pe}) = 10$ (After [Chu \[2004\]](#))

The Loss Cone Maser

Although this kind of interaction was studied in the context of wave amplification at least 50 years ago, it became interesting only after realization that relativistic corrections to the particle distributions were necessary to obtain realistic theoretical predictions, even for weakly relativistic electrons. *Wu and Lee* [1979] introduced this idea and proposed a distribution of electrons energized upwards as result of magnetic reflection as the possible source for wave amplification. Interestingly, the authors considered the possibility of a magnetic field-aligned electric field to explain the nature of the emitted radiation, but did not consider its effect on the electron distribution.

In the auroral zone, incoming particles from the plasma Sheet are either mirrored back to the magnetosphere or precipitated into the atmosphere. At a fixed altitude, the distribution of falling particles has more elements than the distribution of ascending particles. The "missing" particles appear in the phase space as an empty region defined by the local pitch angle (see figure 1.5). The resonance curve (1.1) allows us to understand the importance of the relativistic condition: given the appropriate parameters, a curve with elliptic form overlaps points of the distribution for which $\partial f / \partial v_{\perp} > 0$, rather than the vertical straight line (not shown) that represents the nonrelativistic case.

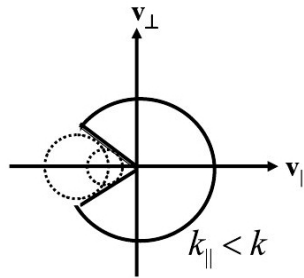


Figure 1.5: Loss cone distribution. The dotted ellipses represent the resonance curve harmonics. (After *Su et al.* [2007])

The Loss Cone Maser provided important improvements with respect to other theories; it explained the predominance of RX mode radiation, (conditioned to emission not perpendicular to the magnetic field (that is, $k_{\parallel} \neq 0$)) and the relaxation of plasma conditions needed for the maser to work. Calculations of growth rates [*Melrose and Dulk*, 1982] were also substantially more accurate. Despite this relative success more accurate spacecraft observations showed important discrep-

ancies related to the frequency spectra of AKR [[Treumann, 2006](#)] (and references within).

The Shell Maser

A major improvement to the Loss Cone Maser was possible once it was solidly established that magnetic field aligned-electric fields at the source region were strong enough to accelerate electrons [[Louarn et al., 1990](#)][[Ergun et al., 2000](#)], thereby introducing an important modification to the particle distribution. The presence of such electric fields decreases the particle density at low energies by accelerating electrons downwards and ions upwards. Downward moving electrons increase their transverse kinetic energy at the expense of their parallel kinetic energy due to magnetic moment conservation. In terms of the phase space distribution, the electric field creates a hole centered at the origin, and the loss-cone distribution evolves into a Horseshoe distribution with $\partial f / \partial v_{\perp} > 0$ like the one sketched in figure 1.6.

[Pritchett \[1984\]](#) found significant differences when comparing the cold plasma case against a distribution of electrons with $(v/c)^2 > (\omega_{pe}/\omega_{ce})^2 \ll 1$; the cold plasma limit predicted a cut-off for the extraordinary mode $\omega_X > \omega_{ce}$, with no chance for perpendicular emission, and maximum growth rates at angles $(10 - 20)^{\circ}$ with respect to the normal direction, whereas in the semirelativistic approach the cut-off is shifted below the electron cyclotron frequency. With this modification, emission in the RX mode is not only possible, but also most intense at $k_{\parallel} = 0$.

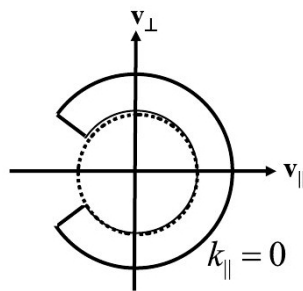


Figure 1.6: Shell distribution and its resonance curve (*After [Su et al. \[2007\]](#)*)

1.3 Alfvén waves as potential sources of AKR

Alfvén waves are a common mechanism of energy redistribution in magnetized plasmas. In the magnetosphere, their origin is often attributed to the solar wind flowing along the magnetopause, which produces surface waves that grow as Kelvin Helmholtz waves. These perturbations launch compressional waves that propagate inside the magnetosphere [*Kivelson and Russell, 1995*]. Other processes associated with Alfvén wave generation are shear flows across the background magnetic field [*Stasiewicz et al., 2000*], or sudden reconfigurations of the magnetic field (e.g., magnetic reconnection, displacement of the magnetopause due to a sudden increase or decrease on the Solar Wind conditions).

Alfvén waves consist of low frequency ($\omega \ll \omega_{ci}$) electromagnetic oscillations propagating in a conducting fluid embedded in an external magnetic field. The restoring force for the waves is provided by the background magnetic field, while the ion mass provides the inertia. These waves play an important role in the coupling of energy between the magnetosphere and the ionosphere. In the collisionless magnetospheric environment, compressional waves often mode convert into shear waves via field line resonances [*Kivelson and Russell, 1995*]. In this process, shear waves travel along magnetic field lines without damping until they arrive at the resistive ionosphere, where magnetic stresses are relaxed through several dissipative processes (and, at regions of $v_A > v_{Te}$, E_{\parallel} decreases and electrons can escape). Some examples are: collisional damping, destructive interference with shear modes reflected at the ionosphere, and the one we are interested in: mode conversion to dispersive waves, which contributes to Joule heating, particle acceleration, and radiation emission [*Cramer, 2001*]. Dispersive modes appear when the perpendicular scale length is comparable to the ion gyroradius corresponding to the ion or electron temperature [*Hasegawa and Chen, 1976*], or to the electron skin depth [*Goertz and Boswell, 1979*]. DAWs have a component of electric field aligned with the background magnetic field, and are therefore able to accelerate particles along magnetic field lines. These accelerated electron distributions can potentially act as a free energy source for AKR.

Next, we explore the existence of DAWs using the two-fluid plasma approximation, and give an expression for the parallel electric field in terms of the perpendicular wave perturbations and the parameters that characterize the local neighbourhood. First of all, we review the theory of ideal MHD waves.

1.3.1 MHD waves

Consider an electrically neutral, highly conducting, nonviscous and compressible plasma, initially in equilibrium in a region with a uniform background magnetic field $\mathbf{B}_0 = B_0 \hat{\mathbf{z}}$. The initial density and pressure are $\rho = n_0 (m_e + m_i) \approx n_0 m_i$ and p_0 , respectively.

A small, low frequency perturbation is excited in this plasma, with the reference system chosen such that the wavenumber is defined by $\mathbf{k} = k_x \hat{\mathbf{x}} + k_z \hat{\mathbf{z}}$, making an angle θ with the external field. The wave propagates with velocity

$$\mathbf{v}(\mathbf{r}, t) = \delta \mathbf{v} = \delta \mathbf{v}_0 e^{i(\mathbf{k} \cdot \mathbf{r} \pm \omega t)} \quad (1.23)$$

As a consequence of the wave disturbance, small perturbations arise in the plasma. These perturbations are assumed to be noticeable only to first order:

$$n(\mathbf{r}, t) = n_0 + \delta n(\mathbf{r}, t) \quad (1.24)$$

$$p(\mathbf{r}, t) = p_0 + \delta p(\mathbf{r}, t) \quad (1.25)$$

$$\mathbf{E}(\mathbf{r}, t) = \delta \mathbf{E}(\mathbf{r}, t) \quad (1.26)$$

$$\mathbf{j}(\mathbf{r}, t) = \delta \mathbf{j}(\mathbf{r}, t) \quad (1.27)$$

$$\mathbf{B}(\mathbf{r}, t) = B_0 \hat{\mathbf{z}} + \delta \mathbf{B}(\mathbf{r}, t) \quad (1.28)$$

In order to find a dispersion relation that describes the nature of the propagating waves, the following physical relations will be used:

- Continuity equation

$$\frac{\partial n}{\partial t} + n \nabla \cdot \mathbf{v} = 0 \quad (1.29)$$

linearization of (1.29) yields

$$\frac{\partial \delta n}{\partial t} + n_0 \nabla \cdot \delta \mathbf{v} = 0 \quad (1.30)$$

- Momentum conservation and low frequency Ampere's law

$$\rho \frac{D\mathbf{v}}{Dt} = -\nabla p + \mathbf{J} \times \mathbf{B} \quad (1.31)$$

$$\nabla \times \mathbf{B} = \mu_0 \mathbf{J} \quad (1.32)$$

Equation (1.32) allows us to eliminate \mathbf{J} from (1.31). Then, using the identity $(\nabla \times \mathbf{B}) \times \mathbf{B} = (\nabla \cdot \mathbf{B}) \mathbf{B} - \nabla \left(\frac{B^2}{2} \right)$ the following equation results

$$n_0 m_i \frac{\partial \delta \mathbf{v}}{\partial t} = -\nabla \left(\delta p + \frac{\mathbf{B}_0 \cdot \delta \mathbf{B}}{\mu_0} \right) + \frac{(\mathbf{B}_0 \cdot \nabla) \delta \mathbf{B}}{\mu_0} \quad (1.33)$$

- Adiabatic energy equation

$$(p\rho^\gamma) = \text{const} \quad (1.34)$$

Time differentiation and linearization yields

$$\begin{aligned} \frac{\partial \delta p}{\partial t} &= -\frac{p_0 \gamma}{n_0} \frac{\partial \delta n}{\partial t} \\ &= m_i n_0 c_s^2 \nabla \cdot \delta \mathbf{v} \end{aligned} \quad (1.35)$$

Where $c_s = \frac{\gamma p_0}{m_i n_0}$ is the velocity of sound, and the time derivative of the density was replaced using (1.30).

- Faraday's Law

$$\nabla \times \mathbf{E} = -\frac{\partial \mathbf{B}}{\partial t} \quad (1.36)$$

- Ohm's law for ideal MHD

$$\mathbf{E} + \mathbf{v} \times \mathbf{B} = \mathbf{0} \quad (1.37)$$

The electric field is eliminated by combining (1.36) and (1.37). The resulting relation can be used to determine the polarization of the magnetic field perturbation (once $\delta \hat{\mathbf{v}}$ is known)

$$\frac{\partial \mathbf{B}}{\partial t} = (\mathbf{B}_0 \cdot \nabla) \delta \mathbf{v} - \mathbf{B}_0 (\nabla \cdot \delta \mathbf{v}) \quad (1.38)$$

Equations (1.33), (1.35) and (1.38) can be combined to obtain a single equation depending on only one of the variables. The momentum equation (1.33) gives,

$$n_0 m_i \frac{\partial^2 \delta \mathbf{v}}{\partial t^2} = -\nabla \left(\frac{\partial \delta p}{\partial t} + \frac{B_0}{\mu_0} \frac{\partial \delta B_z}{\partial t} \right) + \frac{B_0}{\mu_0} \frac{\partial}{\partial z} \left(\frac{\partial \delta \mathbf{B}}{\partial t} \right) \quad (1.39)$$

while time variations of the magnetic field and pressure can be substituted using (1.35) and (1.38) to obtain

$$\frac{\partial^2 \delta \mathbf{v}}{\partial t^2} = -c_s^2 \nabla (\nabla \cdot \delta \mathbf{v}) - v_A^2 \nabla \left(\frac{\partial \delta v_z}{\partial z} - \nabla \cdot \delta \mathbf{v} \right) + v_A^2 \left(\frac{\partial^2 \delta \mathbf{v}}{\partial z^2} - \nabla \cdot \frac{\partial \delta \mathbf{v}}{\partial z} \hat{\mathbf{z}} \right) \quad (1.40)$$

Finally, by assuming a solution varying as (1.23), we obtain an equation for the velocity

$$\left[(\omega^2 - k_z^2 v_A^2) \mathbf{I} - (c_s^2 + v_A^2) \mathbf{k} \mathbf{k} + (\mathbf{k} \hat{\mathbf{z}} + \hat{\mathbf{z}} \mathbf{k}) k_z v_A^2 \right] \cdot \delta \mathbf{v}_0 = 0 \quad (1.41)$$

or, equivalently

$$\begin{bmatrix} \omega^2 - (k_z v_A)^2 - k_x^2 (c_s^2 + v_A)^2 & 0 & -c_s^2 k_x k_z \\ 0 & \omega^2 - (k_z v_A)^2 & 0 \\ -c_s^2 k_z k_x & 0 & \omega^2 - (c_s k_z)^2 \end{bmatrix} \cdot \delta \mathbf{v}_0 = 0 \quad (1.42)$$

The determinant provides the dispersion relation describing three possible wave modes

$$\left[\omega^2 - (k v_A \cos \theta)^2 \right] \left[\omega^4 - \omega^2 k^2 (c_s^2 + v_A^2) + (k^2 v_A c_s \cos \theta)^2 \right] = 0 \quad (1.43)$$

The Shear Alfvén mode

From equation (1.42), there is an uncoupled wave mode for $\delta \mathbf{v}_0 = \delta v_0 \hat{\mathbf{y}}$. The oscillation takes place in a direction perpendicular to both the background magnetic field and the wave vector. The magnitude of the velocity is related directly to the amplitude of the magnetic perturbation, as can be deduced from equation (1.38). By taking

$$\delta \mathbf{B} = \delta \mathbf{B}_0 e^{i(\mathbf{k} \cdot \mathbf{r} \pm \omega t)} \quad (1.44)$$

it is found that the magnetic field also oscillates in the perpendicular plane, an-

tiparallel (parallel) to the velocity perturbation when the wave travels parallel (antiparallel) to the background magnetic field.

$$\delta\mathbf{v}_0 = \mp B_0 \frac{\omega}{k \cos \theta} \delta\mathbf{B} = \mp \frac{v_A}{B_0} \delta\mathbf{B} \quad (1.45)$$

The electric field polarization is, for all modes, perpendicular to the unperturbed magnetic field and the wave vector, see (1.37). In this case

$$\delta\mathbf{E} = \pm v_A \delta\mathbf{B} \times \hat{\mathbf{z}} \quad (1.46)$$

Notice that for this particular case, $\nabla \cdot \delta\mathbf{v} = 0$ and $B^2 \sim B_0^2$ to first order, and thus neither the dynamic nor the magnetic pressures change because of the oscillation. The shear mode induces tangential stresses along the field line intending to restore the magnetic field lines that have been bent from their equilibrium position.

The fast and slow magnetoacoustic modes

The second parenthesis in equation (1.43) reveals two modes associated with waves in the plane defined by the wave vector and the magnetic field; known as *fast* (+) and *slow* (-) magnetosonic or magnetoacoustic waves, respectively. The corresponding phase velocities for these waves are, respectively, defined by

$$\left(\frac{\omega}{k}\right)^2 = \frac{1}{2} \left[v_A^2 + c_s^2 \pm \sqrt{(v_A^2 + c_s^2)^2 - (2v_A c_s \cos \theta)^2} \right] \quad (1.47)$$

The phase velocity for the fast mode has a minimum value of $\max(v_A, c_s)$ when propagating parallel to the background magnetic field, and it takes higher values for increasing inclinations, rising to a maximum value of $\sqrt{v_A^2 + c_s^2}$ for $\theta = \pi/2$. On the other hand, the slow mode has a maximum phase velocity of $\min(v_A, c_s)$ when it propagates parallel to the magnetic field, and it decreases with increasing θ to a minimum value of zero at $\theta = \pi/2$.

The motion of the wave is such that $\delta\mathbf{v}_0 = \delta v_x \hat{\mathbf{x}} + \delta v_z \hat{\mathbf{z}}$, and the magnetic and electric perturbations are given by

$$\delta\mathbf{B} = -\frac{B_0}{\omega} (\mathbf{k} \cdot \delta\mathbf{v} \hat{\mathbf{z}} - k \cos \theta \delta v) \quad (1.48)$$

$$\delta\mathbf{E} = \delta v_x B_0 \hat{\mathbf{y}} \quad (1.49)$$

1.3.2 Dispersive Alfvén Waves (DAW)

When the typical length scale in the plasma is of the same order as the microscopic length, then microscopic behaviour is detectable macroscopically [*Hasegawa and Chen, 1976*]. When the typical perpendicular length is comparable to the difference between the actual and averaged position for a certain particle, then this particle cannot be treated as frozen into the plasma, and consequently one must account for currents perpendicular to the background magnetic field. These currents are provided mostly through polarization drift [*Vogt, 2002*][*Stasiewicz et al., 2000*], which is present in both fast and shear Alfvén waves:

$$\mathbf{j}_\perp = \frac{1}{\mu_0} \frac{d\mathbf{E}_\perp}{dt} \quad (1.50)$$

In order to estimate new wave dispersion properties not present in ideal MHD, inertial and pressure effects must be included in the formulation through Ohm's law. In its linearized form, this is defined by,

$$\delta\mathbf{E} + \delta\mathbf{v} \times \mathbf{B}_0 = \frac{m_e}{n_0 e^2} \frac{\partial \delta\mathbf{j}}{\partial t} - \frac{\nabla \delta p_e}{ne} \quad (1.51)$$

where it has been assumed that the electron temperature is higher than the ion temperature. A constant background magnetic field and $\nabla \cdot \delta\mathbf{v} = 0$ is assumed. Following *Paschmann et al. [2003]*, we consider zero order solutions for $\delta\mathbf{v}$ (1.45) and $\delta\mathbf{E}$ (1.46) in order to find the wave dispersion relation. First of all, we make use of the induction equation and (1.46) to obtain

$$\frac{\partial \delta\mathbf{B}}{\partial t} = \mp v_A \frac{\partial \delta\mathbf{B}}{\partial z} \quad (1.52)$$

Then, using (1.51), we separate the electric field components into components parallel and perpendicular to the magnetic field

$$E_\perp = -\delta\mathbf{v} \times \mathbf{B}_0 = \pm v_A \delta\mathbf{B} \times \hat{\mathbf{z}} \quad (1.53)$$

$$E_\parallel = \frac{m_e}{n_0 e^2} \frac{\partial \delta j_\parallel}{\partial t} - \frac{\partial \delta p_e}{\partial z} \quad (1.54)$$

A relation involving the electron pressure is obtained by multiplying the electron continuity equation by the electron temperature

$$\begin{aligned} \left[\begin{array}{l} \frac{\partial \delta n_e}{\partial t} = -\nabla \cdot \delta \mathbf{v}_e \\ \frac{\partial \delta p_e}{\partial t} = \frac{k_B T_e}{e} \frac{\partial \delta j_{\parallel}}{\partial z} \end{array} \right] \times k_B T_e \end{aligned} \quad (1.55)$$

Hence, we can eliminate the pressure from our system of equations by taking the time derivative of (1.54), yielding

$$\frac{\partial E_{\parallel}}{\partial t} = \frac{m_e}{n_0 e^2} \frac{\partial^2 \delta j_{\parallel}}{\partial t^2} - \frac{k_B T_e}{n e^2} \frac{\partial^2 \delta j_{\parallel}}{\partial z^2} \quad (1.56)$$

The current density is retrieved from Ampere's law, where we neglect the displacement current, which becomes important only when the Alfvén velocity approaches the light velocity (the relativistic case is studied in chapter 2)

$$\begin{aligned} \delta \mathbf{j} &= \frac{1}{\mu_0} \nabla \times \delta \mathbf{B} = \frac{1}{\mu_0} (\nabla_{\perp} + \nabla_{\parallel}) \times \delta \mathbf{B} \\ &= \frac{1}{\mu_0} \left(\frac{\partial(\hat{\mathbf{z}} \times \delta \mathbf{B})}{\partial z} + \nabla_{\perp} \times \delta \mathbf{B} \right) \end{aligned} \quad (1.57)$$

The last equation we need is Faraday's law

$$\frac{\partial \delta \mathbf{B}}{\partial t} = -\nabla_{\parallel} \times \mathbf{E}_{\perp} - \nabla_{\perp} \times \mathbf{E}_{\parallel} = -\frac{\partial(\hat{\mathbf{z}} \times \mathbf{E}_{\perp})}{\partial z} - \nabla_{\perp} \times \mathbf{E}_{\parallel} \quad (1.58)$$

Let us take the time derivative of the induction equation

$$\frac{\partial^2 \delta \mathbf{B}}{\partial t^2} = -\frac{\partial}{\partial z} \left(\hat{\mathbf{z}} \times \frac{\partial \mathbf{E}_{\perp}}{\partial t} \right) - \nabla_{\perp} \times \frac{\partial \mathbf{E}_{\parallel}}{\partial t} \quad (1.59)$$

The first term is found by combining equations (1.53) and (1.52). The second term requires taking the curl of equation (1.56) and substituting the expression $\nabla_{\perp} \times \mathbf{j}_{\parallel} = -\nabla_{\perp}^2 \delta \mathbf{B} / \mu_0$, which comes from taking the curl of Ampere's law. After some straightforward mathematical manipulations, we obtain

$$\frac{\partial^2 \delta \mathbf{B}}{\partial t^2} = v_A^2 \frac{\partial^2 \delta \mathbf{B}}{\partial z^2} + \left(\frac{m_e}{n e^2} \frac{\partial^2}{\partial t^2} - \frac{k_B T_e}{n e^2} \frac{\partial^2}{\partial z^2} \right) \frac{\nabla_{\perp}^2 \delta \mathbf{B}}{\mu_0} \quad (1.60)$$

Fourier analysis of this equation leads to the dispersion relation

$$\left(\frac{\omega}{k_{\parallel}} \right)^2 = v_A^2 \frac{1 + (k_{\perp} \rho_s)^2}{1 + (k_{\perp} \lambda_e)^2} \quad (1.61)$$

where $\rho_s = c\lambda_{De}/v_A$ is the ion acoustic gyroradius and $\lambda_e = c/\omega_{ce}$ is the electron inertial length.

Mechanism of acceleration of particles

Our interest is to find an expression for the parallel electric field, which in this case can be defined in terms of the perpendicular component of the electric field. First of all, notice that

$$\nabla_{\parallel} \cdot \mathbf{j}_{\parallel} = -\frac{1}{\mu_0} \frac{\partial(\nabla_{\perp} \cdot \mathbf{E}_{\perp})}{\partial t} \quad (1.62)$$

which follows from current continuity and the definition of the polarization current, equation (1.50). Now we can differentiate (1.56) twice with respect to the coordinate z to get

$$\frac{\partial^2 \delta E_{\parallel}}{\partial z^2} = \left(-\left(\frac{\lambda_e}{v_A}\right)^2 \frac{\partial^2}{\partial t^2} + \rho_s^2 \frac{\partial^2}{\partial z^2} \right) \frac{\partial(\nabla_{\perp} \cdot \delta \mathbf{E}_{\perp})}{\partial z} \quad (1.63)$$

Finally, we use Fourier analysis to solve for δE_{\parallel}

$$\delta E_{\parallel} = \left(\frac{\rho_s^2 - \lambda_e^2}{1 + (k_{\perp} \lambda_e)^2} \right) \frac{\partial(\nabla_{\perp} \cdot \delta \mathbf{E}_{\perp})}{\partial z} \quad (1.64)$$

Equation (1.64) indicates that pressure and inertial effects act oppositely in contributing to the parallel electric field. In the inertial limit ($\lambda_e > \rho_s$), it accelerates the electrons carrying the parallel current, and decelerates them if pressure effects are more important [*Paschmann et al.*, 2003]. The criteria to determine between the cold and warm regimes is derived from the ratio

$$\frac{\rho_s}{\lambda_e} = \sqrt{\beta_e \frac{m_i}{m_e}} \quad (1.65)$$

The quantity $\beta_e = \mu_0 n k_B T_e / B_0^2$ is known as the electron plasma beta. For the inertial limit $\beta_e < m_e/m_i$, while at the kinetic limit $\beta_e > m_e/m_i$.

Dispersive Alfvén wave's capabilities to accelerate electrons are supported by observations [*Ergun et al.*, 2005] [*Chaston et al.*, 1999]. In general, examination of *in situ* measurements shows evidence of alfvénic activity whenever electric and magnetic perturbations are correlated and are such that $\delta E_{\perp} / \delta B_{\perp} \sim v_A$. Special interest has been focused on IAWs, since the inertial regime covers the lower altitude range up to $3 - 4R_e$ geocentric [*Lysak and Carlson*, 1981], which includes the AKR source region. More accurate descriptions of alfvénic activity have been

provided by the Freja (600 - 1750 km altitude) and FAST (350 - 4180 km altitude) satellites [*Stasiewicz et al.*, 2000]. The low frequency window (1 - 20 Hz) of the electromagnetic spectrum was found to consist of two main elements [*Louarn et al.*, 1994]: 1. quasistatic magnetic fluctuations with no electric nor density counterpart, associated with stationary currents, and 2. Solitary Kinetic Alfvén Waves (SKAW): usually a single electric pulse of high amplitude, clearly identified as alfvénic for which the ratio of electric and magnetic amplitudes is close to the Alfvén speed, accompanied by a strong density perturbation and large Poynting flux. Later studies reported similar features [*Ergun et al.*, 1998] [*Chaston et al.*, 2000] [*Chaston et al.*, 2002] [*Stasiewicz et al.*, 2000] and gave a more detailed description based on FAST measurements. SKAW electric amplitudes were found to range from 100 – 500 mV/m, magnetic ones from: 30 – 100 nT; with associated density depletions up to $\Delta n/n = 100\%$ over a very short bandwidth of < 1 kHz. With each SKAW, *Chaston et al.* [2000] identified an accompanying electron flux spanning the range of low electron energies; this feature is known as Suprathermal Electron Burst (STEB).

Numerical simulations of IAW wave pulses along a constant magnetic field found that inertial effects will accelerate resonant electrons to final velocities $v_f \sim 2v_A - v_i$ (v_i is the initial velocity), and postulated a proportional relation between the energy of the accelerated electrons and the perpendicular wavelength [*Kletzing*, 1994]. *Watt et al.* [2004] corroborated this behaviour using a self-consistent approach, and also found that an enhancement on the number of accelerated particles as a consequence of the modification of the electric field profile due to particle-wave interactions.

Chapter 2

Test Particle and Wave Algorithms

In this chapter, the equations solved by the wave-particle interaction model are introduced, and a detailed statement of the simplifying assumptions is supported by a theoretical discussion of the basics of particle motion and wave propagation considering inertial effects. Numerical issues are addressed and a comparison between the analytical and numerical wave dispersion relation determines the condition that guarantees the physically accurate wave propagation.

The presence of a constant background magnetic field tends to organize the motion of charged particles by making them move around magnetic field lines and confining them to a particular flux tube over a certain timescale. However, the problem of the temporal behaviour of a plasma is in general very complex unless assumptions are made to disregard the less important elements. In particular, a self-consistent approach implies that particles moving according to external fields are allowed to affect the original fields, implying a direct coupling between particles and fields through Maxwell's equations. The new configuration of fields will affect particles in a different way, and the evolution of the particle motion must be reformulated to consider the new configuration. A self-consistent particle code requires a closed system with a number of equations describing particle-particle and wave-particle interactions. In the most general case, precise knowledge of all particle positions and velocities is necessary in three dimensions, which rapidly becomes intractable, except perhaps using the largest computers currently available.

Instead of the three-dimensional approach, a one-dimensional test particle code has been written based only on wave-particle interactions. As pointed out in the introductory chapter, it is of general understanding that emission of AKR is fed

by the free energy stored in the distribution of particles with $\partial f / \partial v_{\perp} > 0$. The interest in this thesis is to determine the magnetospheric and Alfvén wave conditions that produce appropriate unstable distributions in the AKR source region. The algorithm to be presented has been formulated to allow particle distributions to develop spontaneously by simulating the time evolution of a number of particles upon interaction with Inertial Alfvén waves (IAWs). This approach is valid on the typical timescales of wave propagation (seconds) and under the assumption that a small amount of energy is extracted from the wave during its interaction with electrons. This implies that the feedback of particles on the wave fields can be neglected to first order.

Since collisions in magnetospheric plasma are very rare, they are neglected in the formulation of the problem at hand. Additionally, the short timescales of interest, imply that the three-dimensionality of the space-phase configuration is no longer required. Reduction of the number of dimensions is a desirable feature that translates into a reduced number of equations to be solved, which means less computational resources per particle. Additionally, conservation of the first adiabatic invariant (and consequently, magnetic flux conservation) for the electrons is required. Conservation of magnetic moment allows to preserve knowledge of the perpendicular velocity despite the dimensionality reduction, while flux conservation is used to approximate the propagation properties at any position of the computational domain, given a reference point at which such properties are known. These simplifications allow getting a closed system of equations that can be solved in time numerically, and for which a reasonable amount of computational resources is needed. On the other hand, part of the physics is lost in the formulation: the model is unable to reproduce wave damping and growing, as well as to ensure energy conservation.

The model includes inhomogeneity of the background magnetic field, which is an important feature that introduces the magnetic mirror force, while any IAWs that are present are allowed to vary their speed, amplitude and spatial extent. Since the basic wave-particle interaction of interest involves particles surfing on wave fronts, all these effects are important. For example, if particles are accelerated to move ahead of the wave, their streaming motion may once again be affected as the wave catches up with the particle on the inhomogeneous plasma along which it moves. The general rule for the neglect of 2d effects can be defined from the perpendicular displacement that a particle with given energy and pitch angle undergoes in one bounce along the magnetic line. Such a displacement is, for a given drift velocity

V_D

$$X = 2 \int_0^\pi ds \frac{V_D}{v_{\parallel}} \quad (2.1)$$

There are various drift velocities that occur in an inhomogeneous plasma; drift velocities caused by gradient and curvature of the ambient magnetic field are derived later in equation (2.25) and (2.26). Their combined effect is summarized as [Baumjohann and Treumann, 1997]

$$\mathbf{v}_D = \mathbf{v}_c + \mathbf{v}_\nabla = \left(v_{\parallel}^2 + \frac{v_{\perp}^2}{2} \right) \frac{\mathbf{B} \times \nabla B}{\omega_c B^2}. \quad (2.2)$$

The model discussed here discards particle drifts as a possible sink of particles along a magnetic field line. Therefore, an estimation of how much this drift can be on a time scale of a bounce period is needed. In order to get such an estimation, we use a dipolar description for the magnetic field, expressed in spherical coordinates [Baumjohann and Treumann, 1997]

$$\mathbf{B}(r, \theta) = \frac{\mu_0 M_E}{4\pi r^3} \left(2 \cos \theta \hat{\mathbf{r}} + \sin \theta \hat{\theta} \right) \quad (2.3)$$

where $M_E = 8.05 \times 10^{22} \text{ Am}^2$ is the dipolar magnetic moment. The magnitude of the magnetic field is

$$B(r, \theta) = \frac{\mu_0 M_E}{4\pi r^3} (1 + 3 \cos^2 \theta)^{1/2} \quad (2.4)$$

The value of the r coordinate along the field line can be given in terms of the axial coordinate and the radial distance of the equator r_{eq}

$$r = r_{eq} \cos^2 \theta \quad (2.5)$$

Substitution of these three last expressions into (2.2) leads to the following equation for the drift velocity caused by nonuniformity of the magnetic field

$$\mathbf{v}_D = 12 \frac{m\pi r_{eq}^2}{q\mu_0 M_E} \left(v_{\parallel}^2 + \frac{v_{\perp}^2}{2} \right) \frac{\cos \theta (1 + \sin^2 \theta)}{(1 + 3 \sin^2 \theta)^2} (-\hat{\mathbf{z}}) \quad (2.6)$$

for which an upper limit can be set up in terms of the initial kinetic energy K

$$v_{Dmax} < 24\pi \frac{r_{eq}^2 K}{q\mu_0 M_E} \quad (2.7)$$

The bounce period of a particle trapped in the magnetic field is approximated as

[[Baumjohann and Treumann, 1997](#)]

$$\begin{aligned}\tau_b &= 4 \int_0^{\pi/2} d\theta \frac{ds}{v_{\parallel}} \\ &\simeq r_{eq} \sqrt{\frac{m}{K}} (3.7 - 1.6 \sin \alpha_{eq})\end{aligned}\quad (2.8)$$

Here α_{eq} is the particles pitch angle at the equator.

The maximum deviation of an electron in one bounce period is always less than the distance

$$v_{Dmax} \times \tau_b(\alpha_{eq} = 0) = \frac{3.7 \times 6 \times 10^7 r_{eq}^3 \sqrt{mK}}{qM_E} \quad (2.9)$$

A more realistic estimation requires formal integration of

$$\int_0^{\tau} dt \mathbf{v}_D \quad (2.10)$$

For a typical electron with energy $K = 1$ keV moving close to the magnetic field line at $r_{eq} = 5R_E$, this maximum deflection has an approximate value of 6.8 km, which can be considered not too big for the space scales of the problem, but grows rapidly with L . To further justify the 1 dimensional formulation for magnetic field lines close to the Earth, we can take advantage of the cylindrical symmetry of the dipolar magnetic field around the Earth; due to this symmetry, for any particle leaving the system due to magnetic drifts there should be an identical particle incoming for the same reason.

2.1 Basic particle motion in externally applied fields

The model to be described later is required to approximate every particle's dynamic state by solving the Lorentz equation

$$m_s \frac{d\mathbf{v}}{dt} = q_s (\mathbf{E} + \mathbf{v} \times \mathbf{B}) \quad (2.11)$$

for which it is necessary to know the value of the electric and magnetic fields at the position of the particle, as well as its velocity. It is worth to study equation (2.11) for a few special cases that provide insight on how particles react in the presence of electromagnetic fields.

2.1.1 Motion due to a constant electric field

A positive (negative) charged particle in a constant electric field and with zero magnetic field will accelerate uniformly in the direction parallel (antiparallel) to the field. The magnitude of the acceleration is, according to (2.11)

$$\frac{d\mathbf{v}}{dt} = \frac{q_s}{m_s} \mathbf{E} \quad (2.12)$$

2.1.2 Motion due to a constant magnetic field

To explain the effect of a magnetic field on charged particle motion, choose a reference system for which one of the axes is also the (parallel) direction of the magnetic field \mathbf{b} . In this system the velocity can be expressed as

$$\mathbf{v} = v_{\parallel} \mathbf{b} + \mathbf{v}_{\perp}. \quad (2.13)$$

Notice that if the velocity were parallel to the magnetic field, (2.11) predicts no acceleration, and therefore this component is a constant of motion. On the other hand, if the velocity is orthogonal to the magnetic field the resulting acceleration is perpendicular to both \mathbf{v}_{\perp} and \mathbf{b} . For this special case the vectorial product of (2.11) with the magnetic field yields the following equation

$$m_s \frac{d(\mathbf{v}_{\perp} \times \mathbf{B})}{dt} = q_s B^2 ((\mathbf{b} \cdot \mathbf{v}_{\perp}) \mathbf{b} - (\mathbf{b} \cdot \mathbf{b}) \mathbf{v}_{\perp}) \quad (2.14)$$

Here the vectorial identity $\mathbf{A} \times (\mathbf{B} \times \mathbf{C}) = \mathbf{B}(\mathbf{A} \cdot \mathbf{C}) - \mathbf{C}(\mathbf{A} \cdot \mathbf{B})$ has been used. Substituting the term $\mathbf{v}_{\perp} \times \mathbf{B}$ from the original Lorentz equation, provides

$$\frac{d^2 \mathbf{v}_{\perp}}{dt^2} + \left(\frac{q_s B}{m_s} \right)^2 \mathbf{v}_{\perp} = 0. \quad (2.15)$$

On defining $\Omega_s = q_s B / m_s$, and substituting the velocity in terms of the position, this equation can be rewritten as

$$\frac{d}{dt} \left[\frac{d^2 \mathbf{r}_{\perp}}{dt^2} + \Omega_s^2 \mathbf{r}_{\perp} \right] = 0 \quad (2.16)$$

or, upon integration

$$\frac{d^2(\mathbf{r}_{\perp} - \mathbf{r}_0)}{dt^2} + \Omega_s^2(\mathbf{r}_{\perp} - \mathbf{r}_0) = 0 \quad (2.17)$$

Solution to equation (2.17) represents the circular trajectory of a particle around the point \mathbf{r}_0 , with angular velocity Ω_s . The radius of the orbit is commonly called

gyroradius and is such that $v_{\perp} = r_s \Omega_s$

$$r_s = \frac{m_s v_{\perp}}{q_s B} \quad (2.18)$$

A gyrating particle is physically equivalent to a circular electrical circuit from which a current $I = q_s/(2\pi r_s/v_{\perp})$ flows continuously. Then it can be associated a magnetic moment with magnitude

$$|\mu| = IA = \frac{q_s v_{\perp}}{2\pi r_s} \pi r_s^2 = \frac{m_s v_{\perp}^2}{2B} = \frac{K_{\perp}}{B} \quad (2.19)$$

where the last form writes the expression in terms of the kinetic energy associated with the perpendicular velocity and the magnitude of the magnetic field.

In most circumstances, it is not necessary to know the exact location of a particle, and only its trajectory and velocity averaged over one gyration period (gyromotion) is of interest. For a particle whose velocity is perpendicular to a constant and uniform magnetic field, the averaged position is just the point \mathbf{r}_0 and the averaged velocity is zero. If there is a velocity component parallel to the magnetic field, the mean trajectory would be given by $\mathbf{r}_g(t) = \mathbf{r}_0 + v_{\parallel} t \mathbf{b}$, with average velocity $\mathbf{v}_g(t) = v_{\parallel} \mathbf{b}$; the real path followed by the particle consists of a helicoidal trajectory centered at \mathbf{r}_0 around the \mathbf{b} axis. Helicoidal trajectories suggest the use of cylindrical polar coordinates to describe particle motion, with the background magnetic field aligned perpendicularly to the polar plane ($\mathbf{b} = \hat{\mathbf{z}}$, $\mathbf{v}_{\perp} = \hat{\theta}$).

2.1.3 More complicated particle drifts

More complicated electromagnetic fields induce consequences in the particle motion that are not straightforwardly explained from the simple cases given above. For example, consider the situation when, besides the uniform magnetic field, there is also a constant electric field oriented perpendicular to the background magnetic field. For a certain, new reference system moving at constant \mathbf{V} with respect to \mathbf{v}_{\perp} , we can write

$$\mathbf{v}_{\perp} = \mathbf{u}_{\perp} + \mathbf{V} \quad (2.20)$$

so that the equation of motion takes the form

$$m_s \frac{d(\mathbf{u}_{\perp} + \mathbf{V})}{dt} = q_s (\mathbf{E}_{\perp} + \mathbf{u}_{\perp} \times \mathbf{B} + \mathbf{V} \times \mathbf{B}) \quad (2.21)$$

This equation shows that there is a reference system from which the particle appears to perform the circular motion studied previously. The relative velocity of the reference system with respect to the lab system must fulfill the following condition

$$\mathbf{E}_\perp + \mathbf{V} \times \mathbf{B} = \mathbf{0} \quad (2.22)$$

The drift velocity is $\mathbf{V} = \mathbf{E}_\perp \times \mathbf{b}/B$ as can be easily verified by substituting it in (2.22). More generally, any force \mathbf{F} perpendicular to the magnetic field results in a drift of the form

$$\mathbf{V}_\mathbf{F} = \mathbf{F} \times \mathbf{b}/(qB) \quad (2.23)$$

which tends to move the particle perpendicularly to both \mathbf{F} and \mathbf{B} .

Temporal and spatial variations of the fields also engage particle drifts, these being difficult to handle rigorously. Simpler gyro-averaged expressions can be found if changes are noticeable only to first order; a few important cases are:

Curvature force

Since charged particles tend to stick to magnetic field lines, they feel a centrifugal force [*Baumjohann and Treumann, 1997*] when traveling along curved field lines

$$\langle \mathbf{F}_\mathbf{c} \rangle = \frac{m_s v_\parallel^2}{r} (-\hat{\mathbf{r}}) \quad (2.24)$$

where r stands for the instantaneous curvature radius, and the minus sign indicates that the force is directed to the center of curvature. The drift velocity due to this force arises from consideration of (2.23)

$$\mathbf{V}_\mathbf{c} = \frac{2K_\parallel}{q(rB)^2} \mathbf{B} \times \mathbf{r} \quad (2.25)$$

Gradient force

Variation of the magnetic field with position exerts an effective force on particle. In the reference frame of the moving particle, the magnetic field is changing with time, which changes the instantaneous force producing an irregular trajectory. The average force when the change in magnetic field magnitude is small in one gyration is

$$\langle \mathbf{F}_\nabla \rangle = -|\mu| \nabla B \quad (2.26)$$

This force produces, according to (2.23), a drift velocity given by

$$\mathbf{V}_\nabla = \frac{K_\perp}{qB^3} \mathbf{B} \times \nabla B \quad (2.27)$$

2.1.4 Magnetic moment and flux conservation

An important simplification in the study of particle trajectories arises as a consequence of kinetic energy conservation of charged particles when affected by a magnetic force. Consider the parallel movement as described by the gradient force in equation (2.26), which multiplied by $v_\parallel = dz/dt$ becomes

$$m_s v_\parallel \frac{dv_\parallel}{dt} = -|\mu| \frac{dB}{dz} \frac{dz}{dt} \quad (2.28)$$

$$\frac{d(\frac{1}{2}m_s v_\parallel^2)}{dt} = -\frac{m_s v_\perp^2}{2B} \frac{dB}{dt} \quad (2.29)$$

On the other hand, parallel and perpendicular energies are coupled through kinetic energy conservation

$$\frac{dK}{dt} = \frac{dK_\parallel}{dt} + \frac{dK_\perp}{dt} = 0 \quad (2.30)$$

which implies $dK_\parallel/dt = -dK_\perp/dt$. This allows to arrange (2.29) as

$$\frac{1}{\frac{1}{2}m_s v_\perp^2} \frac{d(\frac{1}{2}m_s v_\perp^2)}{dt} - \frac{1}{B} \frac{dB}{dt} = 0 \quad (2.31)$$

The last equation can also be written as

$$\frac{d \ln(\frac{1}{2}m_s v_\perp^2)}{dt} - \frac{d \ln(B)}{dt} = 0 \quad (2.32)$$

from which the following condition arises

$$\frac{K_\perp}{B} = \text{const} \quad (2.33)$$

Magnetic moment conservation is a common approximation used in plasmas. This condition holds as far as the variation of the magnetic field magnitude is negligible in a time interval of one gyroperiod. Along with it, also the magnetic flux (Φ_m) that crosses the area enclosed by the circular trajectory of the particle is constant for every gyration, with a value equal to

$$\Phi_m = \int \mathbf{B} \cdot d\mathbf{A} = \pi r_c^2 B = \frac{2\pi m_s}{q^2} |\mu| \quad (2.34)$$

2.2 Wave propagation

Wave solutions in the inertial regime can be found by considering a neutral plasma constituted by single charged ions and electrons. Take the momentum equation

$$\frac{d\mathbf{u}_s}{dt} = \frac{q_s}{m_s} (\mathbf{E} + \mathbf{u}_s \times \mathbf{B}) - \frac{1}{m_s n_s} \nabla p_s \quad (2.35)$$

and Maxwell's equations

$$\nabla \times \mathbf{E} = -\frac{\partial \mathbf{B}}{\partial t} \quad (2.36)$$

$$\nabla \times \mathbf{B} = \mu_0 \mathbf{j} + \frac{1}{c^2} \frac{\partial \mathbf{E}}{\partial t} \quad (2.37)$$

The electric and magnetic fields can be given in terms of scalar and vector potentials. Assuming the low β approximation, valid in the inertial Alfvén regime, the perpendicular component of the vector potential can be neglected [*Stasiewicz et al., 2000*] ($\mathbf{A} = A\hat{\mathbf{z}}$). The electric and magnetic perturbations are then

$$\mathbf{E} = -\nabla\phi - \frac{\partial A}{\partial t} \hat{\mathbf{z}} \quad (2.38)$$

$$\mathbf{B} = \nabla \times \mathbf{A} = \nabla A \times \hat{\mathbf{z}} \quad (2.39)$$

For low frequency waves, currents perpendicular to the magnetic field can be accounted for through particle drifts [*Stasiewicz et al., 2000*]. Drifts due to the presence of an electric field do not cause charge separation, and therefore, do not contribute to the current. To a first order approximation, however, there is a polarization drift $\mathbf{u}_{\text{ps}} = m_s/(q_s B_0^2) d\mathbf{E}_\perp/dt$, proportional to the mass/charge ratio of the particle. It is the polarization drift that provides most of the perpendicular current

$$\mathbf{j}_\perp \approx nq_i \mathbf{u}_{\text{ps}} = \frac{nm_i}{B_0^2} \frac{d\mathbf{E}_\perp}{dt} = \frac{1}{\mu_0 V_A^2} \frac{d\mathbf{E}_\perp}{dt} \quad (2.40)$$

The total current is obtained from Amperes law, which in terms of the field potentials is

$$\mu_0 \mathbf{j} = \nabla \frac{\partial A}{\partial z} - \nabla^2 A \hat{\mathbf{z}} + \frac{1}{c^2} \frac{\partial}{\partial t} \left(\nabla \phi + \frac{\partial A}{\partial t} \hat{\mathbf{z}} \right) \quad (2.41)$$

Consider now particle motion parallel to the magnetic field, where inertial ef-

fects take place. The motion equation in the parallel direction reads

$$\frac{\partial u_{s\parallel}}{\partial t} = \frac{q_s}{m_s} \left(E_{\parallel} + (\mathbf{u}_s \times \mathbf{B})_{\parallel} \right) \quad (2.42)$$

The second term in the right hand side is obviously zero. Given the difference in mass between different species, it is clear that most of the parallel current is carried by the electrons. In this expression, substitute E_{\parallel} from (2.38) and the electron velocity in terms of the parallel current to get

$$\frac{\partial j_{\parallel}}{\partial t} = -\frac{ne^2}{m_e} \left(\frac{\partial \phi}{\partial z} + \frac{\partial A}{\partial t} \right) \quad (2.43)$$

Finally, calculate j_{\parallel} using (2.41) to obtain

$$\left(1 + \left(\frac{\lambda_e}{c} \right)^2 \frac{\partial^2}{\partial t^2} \right) \frac{\partial \phi}{\partial z} + \left(1 - \lambda_e^2 \nabla_{\perp}^2 + \left(\frac{\lambda_e}{c} \right)^2 \frac{\partial^2}{\partial t^2} \right) \frac{\partial A}{\partial t} = 0 \quad (2.44)$$

where $\lambda_e = c/\omega_{pe}$. Both terms proportional to $(\lambda_e/c)^2$ are very small and can be neglected. A Fourier transform in the perpendicular spatial coordinate leads to

$$\frac{\partial \phi}{\partial z} + \left(1 + (\lambda_e k_{\perp})^2 \right) \frac{\partial A}{\partial t} = 0 \quad (2.45)$$

Regarding the transverse direction, we use $E_{\perp} = -\nabla_{\perp} \phi$ from (2.38), j_{\perp} from (2.40) and substitute into the perpendicular component of (2.41), to obtain, after some algebra

$$\frac{V_A^2 + c^2}{V_A^2 c^2} \frac{\partial \phi}{\partial t} + \frac{\partial A}{\partial z} = 0 \quad (2.46)$$

Differentiating equation (2.45) in time and substituting into (2.46), and assuming plane wave solutions, the dispersion relation for IAWs is found

$$\left(\frac{\omega}{k_{\parallel}} \right)^2 = \frac{(V_A c)^2}{(1 + (k_{\perp} \lambda_e)^2) (V_A^2 + c^2)} \quad (2.47)$$

From the derivations provided above, the equations that describe wave propagation in the inertial (cold plasma) regime are thus defined by

$$c^2 \alpha \frac{\partial A_{\parallel}}{\partial z} + \frac{\partial \phi}{\partial t} = 0 \quad (2.48)$$

$$\beta \frac{\partial A_{\parallel}}{\partial t} + \frac{\partial \phi}{\partial z} = 0 \quad (2.49)$$

where quantities α and β have been introduced, and defined by:

$$\alpha = \frac{V_A^2}{V_A^2 + c^2} \quad (2.50)$$

$$\beta = 1 + k_{\perp}^2 \lambda_e^2 \quad (2.51)$$

2.3 Numerical Algorithm

A 1-D coordinate system with coordinate s is defined along the magnetic field line. Quantities physically defined in all points of space (wave fields and potentials) are represented discretely in the spatial domain at points separated by a distance Δs , except for the background magnetic field, which is assumed constant in time and obeys a given analytic function of position. On the other hand, all particle properties (position, velocity, mass, charge, etc.) are not discretized and can have any value. Extrapolation techniques are then used to estimate discretized field quantities at particle locations, and these are used to calculate the trajectories of the particles.

The magnetic moment μ_e is assumed constant in the numerical Algorithm. Computationally, its value must be calculated each time a particle is created, consistent with its initial energy and position.

The posed problem corresponds to an Initial Value Problem with conditions at the boundaries. The wave equation is already given as a system of two first order partial differential equations. In order to maintain second order accuracy we use centered finite differences to approximate derivatives

$$\frac{\partial f(s_i)}{\partial s} \approx \frac{f(s_{i+1}) - f(s_{i-1})}{2\Delta s} \quad (2.52)$$

Note that this approximation agrees with the formal definition as $\Delta s \rightarrow 0$. With this in mind, and considering that the quantity we need from the potentials (electric field) depends on the gradient of the scalar potential, we can increase the accuracy of our calculations maintaining the amount of storage needed; if we decide to *leap frog* the potentials in space and time, then we can have twice as many discrete points, the only drawback being that we have do not have simultaneous knowledge of the two potentials at the same place, but this is not necessary in this particular case.

Field quantities are represented by numerical arrays. The values of the array at position m and iteration n for the scalar potential, the vector potential and the

electric field, respectively, are such that

$$\begin{aligned} sp_n[m] &\rightarrow \Phi((m - 1/2)\Delta s, (n - 1/2)\Delta t) \\ vp_n[m] &\rightarrow A_{\parallel}(m\Delta s, n\Delta t) \\ ef_n[m] &\rightarrow E_{\parallel}(m\Delta s, (n - 1/2)\Delta t) \end{aligned}$$

$m = 0, 1, 2, \dots, n = 0, 1, 2, \dots$, see figure 2.1.

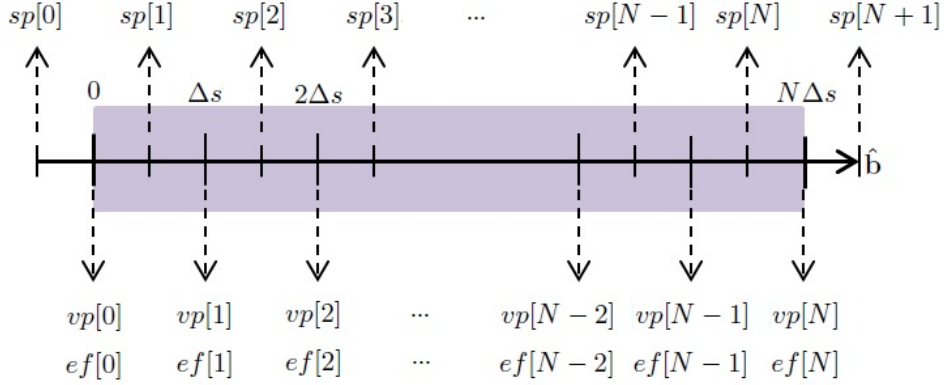


Figure 2.1: Discretization scheme. Scalar and vector potentials are leap-frogged in space (and time). The electric field is at every iteration calculated in the same locations at which the vector potential is defined.

2.3.1 Wave discretization

By applying the definition (2.52) and the discretization shown above to the equation (2.48), an algebraic version is obtained:

$$\alpha c^2 \frac{A_m^n - A_{m-1}^n}{\Delta s} + \frac{\Phi_{m-1/2}^{n+1/2} - \Phi_{m-1/2}^{n-1/2}}{\Delta t} = 0 \quad (2.53)$$

which can be rearranged to get the update equation for the parallel component of the scalar potential:

$$\Phi_{m+1/2}^{n+1/2} = \Phi_{m+1/2}^{n-1/2} - \alpha c^2 \frac{\Delta t}{\Delta s} (A_{m+1}^n - A_m^n) \quad (2.54)$$

The update equation for the vector potential is obtained by following the same procedure with equation (2.49); it turns out to be:

$$A_m^{n+1} = A_m^n - \frac{1}{\beta} \frac{\Delta t}{\Delta s} (\Phi_{m+1/2}^{n+1/2} - \Phi_{m-1/2}^{n+1/2}) \quad (2.55)$$

Since particles are assumed to not influence the wave, equations (2.54) and (2.55) form by themselves a model of wave propagation that only requires the specification of initial and boundary conditions for both of the potentials. Then we can advance this system to any moment in time, a feature that is exploited when calculating particle trajectories, as we will see.

2.3.2 Wave Dispersion Analysis

Analytic Dispersion Relation

The equations (2.48) and (2.49), when combined lead to the wave equation that was obtained previously. Differentiation of (2.48) with respect to time and substitution of the time derivative of the vector potential from (2.49) yields

$$\frac{\partial^2 \Phi}{\partial t^2} - \frac{\alpha c^2}{\beta} \frac{\partial^2 \Phi}{\partial s^2} = 0 \quad (2.56)$$

A solution of the form $\Phi(s, t) = \Phi_0 e^{i(k s \pm \omega t)}$ gives the following dispersion relation

$$\left(\frac{\omega}{k}\right)^2 = \frac{\alpha c^2}{\beta} \quad (2.57)$$

Numerical Dispersion Relation

In the same fashion, a numerical dispersion relation is obtained from the following relations

$$\alpha c^2 \frac{A_m^n - A_{m-1}^n}{\Delta s} + \frac{\Phi_{m-1/2}^{n+1/2} - \Phi_{m-1/2}^{n-1/2}}{\Delta t} = 0 \quad (2.58)$$

$$\beta \frac{A_m^{n+1} - A_m^n}{\Delta t} + \frac{\Phi_{m+1/2}^{n+1/2} - \Phi_{m-1/2}^{n+1/2}}{\Delta s} = 0 \quad (2.59)$$

In this case wave solutions are assumed to be

$$\Phi(s, t) = \Phi_0 e^{i(k(m-1/2)\Delta s \pm \omega(n-1/2)\Delta t)} \quad (2.60)$$

$$A(s, t) = A_0 e^{i(km\Delta s \pm \omega n\Delta t)} \quad (2.61)$$

Substitution of such solutions in the first equation, yields after some algebra

$$\frac{\Phi_0}{A_0} = \alpha c^2 \frac{\Delta t \sin(k\Delta s/2)}{\Delta s \sin(\omega\Delta t/2)} \quad (2.62)$$

The same procedure using the second equation leads to

$$\frac{\Phi_0}{A_0} = \beta \frac{\Delta s \sin(\omega\Delta t/2)}{\Delta t \sin(k\Delta s/2)} \quad (2.63)$$

Equating both equations leads to

$$\left(\frac{\Delta s}{\Delta t}\right)^2 = \frac{\alpha c^2}{\beta} \left(\frac{\sin(k\Delta s/2)}{\sin(\omega\Delta t/2)}\right)^2 \quad (2.64)$$

which can be further rearranged as

$$\left(\frac{\omega}{k}\right)^2 = \frac{\alpha c^2}{\beta} \left(\frac{\text{sinc}(k\Delta s/2)}{\text{sinc}(\omega\Delta t/2)}\right) \quad (2.65)$$

Comparison of the last equation with (2.57) shows that the numerical wave will behave identically to the real one depending on how well the following condition is fulfilled

$$k\Delta s = \omega\Delta t \quad (2.66)$$

2.3.3 Electric field interpolation

The electric field is related to the scalar and vector potentials according to equation (2.38). By substituting the term $\partial A/\partial t$ from (2.49), we obtain a computationally less expensive expression:

$$E(s, t) = \left(\frac{1}{\beta(s)} - 1\right) \frac{\partial \Phi(s, t)}{\partial s} \quad (2.67)$$

The electric field depends ultimately on the gradient of the scalar potential. Its numerical representation is defined on the same temporal points as the scalar potential, and on the same spatial points of the vector potential. The update form of (2.67) is easily found to be

$$E_m^{n+1/2} = \left(\frac{1}{\beta} - 1\right) \frac{\Phi_{m+1/2}^{n+1/2} - \Phi_{m-1/2}^{n+1/2}}{\Delta s} \quad (2.68)$$

What we need, however, is the value of the electric field at the position of every particle. Whatever this position is, it is in-between two points where the electric field has been calculated using (2.68); the electric field at the position of the particle can then be approximated by linear interpolation from these two closest electric field entries of the computational array. In summary, the electric field at an arbitrary position is calculated from the three closest known scalar potentials.

2.3.4 Background Plasma and Magnetic Field

As evidenced in equations (2.45) and (2.46), dispersion properties of waves are modulated by the local medium the waves are propagating into ($k_{\perp}\lambda_e$ and V_A). Magnetic field and particle density dependence in space must be specified in order to calculate the Alfvén velocity, which determines $\alpha(s)$ uniquely (see equation 2.50). The skin depth (inertial scale) for electrons can be calculated from the background density, but further information is required to specify the perpendicular component of the wavenumber. Strictly speaking, Fourier analysis is not rigorously correct for the perpendicular coordinate, but to account for spatial scaling of the wave along a magnetic flux tube, magnetic flux conservation is used to scale k_{\perp} to first order accuracy is assumed. A typical radius of $\lambda_I = 4$ km for the flux tube is taken for the ionosphere, and then $k_{\perp}(s)$ is defined by:

$$k_{\perp}(s) = \frac{2\pi}{\lambda_I} \left(\sqrt{\frac{B(s)}{B_I}} \right) \quad (2.69)$$

A few substitutions more lead to the corresponding expression for $\beta(s)$:

$$\beta(s) = 1 + \left(\frac{2\pi}{\lambda_I} \right)^2 \frac{m_i m_e V_A(s)^2}{B_I e^2 B(s)} \quad (2.70)$$

In the numerical model, the influence of the local background properties is introduced in the wave equations through the $\alpha(\rho(s), B(s))$ (2.50) and $\beta(B(s))$ (2.51) parameters, which ultimately depend on the position, assuming background conditions of magnetic field and density are constant in time. Both homogeneous and inhomogeneous density conditions have been explored and are reported as part of this thesis.

In the homogeneous case, the parameters α and β can be chosen according to the spatial and temporal discretization to satisfy the condition (2.66), which enforces the condition that optimizes physical faithfulness of the numerical wave propagation, so it corresponds exactly to the analytic case. By giving to α (β) some

convenient value, β (α) can be obtained using (2.57). If, on the other hand, density and magnetic field change in space, one can find the location where the maximum wave velocity is expected, and find the interval of possible time discretization that do not violate the Courant condition.

Single wave pulse input

Incorporation of a wave pulse into the computational domain is performed by locating it initially just outside one of the boundaries. The wave is injected through the boundaries by specifying $sp_n[0]$ and $vp_n[0]$ and advancing the wave numerically at each time step. Typically, the incoming pulse has the following shape

$$\begin{aligned}\phi(s, t) &= \phi_0 [1 - \cos(k_{\parallel}s - \omega t)] \\ sp_n[0] &= \phi_0 [1 - \cos(\omega n dt)]\end{aligned}\quad (2.71)$$

The value of the vector potential is approximated by a first order Taylor expansion:

$$\begin{aligned}A_{\parallel}(s, t) &= A_0 + dt \frac{dA}{dt} = A_0 + dt \left(-\frac{1}{\beta} \frac{d\phi}{ds} \right) \\ vp[0] &= vp_{n-1}[0] - \phi_0 k_{\parallel} \frac{\sin(\omega(n + .5)dt)}{\beta} dt\end{aligned}\quad (2.72)$$

2.3.5 Background Magnetic Field

Earth's magnetic field configuration has been extensively studied. A common approximation of the dipolar field as a function of latitude and distance from the Earth (defined through the parameter $L = r/R_e$) is [*Baumjohann and Treumann, 1997*]

$$B(\lambda, L) = \frac{B_E}{L^3} \frac{\sqrt{1 + 3 \sin^2 \lambda}}{\cos^6 \lambda} \quad (2.73)$$

where $B_E = 3.11 \times 10^{-5}$ T. This expression, though easily manageable computationally, is not so convenient when it comes to other quantities of interest. For example, the bounce period for a particle trapped in the magnetic field is a complicated expression with high computational overhead. In order to avoid such inconveniences, the following even simpler expression for the background magnetic

field has been implemented

$$B(s) = B_0 \left[1 + \left(\frac{s}{s_0} \right)^2 \right] \quad (2.74)$$

The parameters B_0 and s_0 are chosen to make magnetic field values at the equator and at the surface of the Earth coincide with values given by (2.73). The coordinate s represents the distance along the field line measured from the equator to the position where the magnetic field is measured. Notice also that particles escaping from the dipolar field will also escape from the magnetic bottle and vice-versa.

An inhomogeneous background density is applied in certain simulations, and is intended to resemble the physical domain ranging from the magnetospheric equator to the ionosphere along a magnetic field line. A simplified choice of density profile emulates an atmosphere composed of oxygen and hydrogen, their concentrations obeying the hydrostatic pressure law and an exospheric law, respectively, according to *Thompson and Lysak* [1996]

$$n(s) = n_O e^{-z/L_o} + n_H \left(\frac{r}{R_E} \right)^{-\gamma}. \quad (2.75)$$

The parameter values and their meanings are described in the original article. Here $r = R_E L \cos \lambda$ and $z = r - R_E$.

2.3.6 Test particle dynamics

The motion of particles is given by Newton's equation of motion (2.11). The magnetic force along the magnetic field is calculated as resulting from the inhomogeneity of the magnetic field, by means of equation (2.26)

$$m_e \frac{dv_{\parallel}}{dt} = -eE_{\parallel}(s, t) - \mu_e \frac{\partial B(s)}{\partial s} \quad (2.76)$$

where μ_e is the magnetic moment for the electron. In the numerical Algorithm, the second term in (2.76) is easily calculated through an analytical expression. The term involving the electric field, however, needs to be approximated numerically, since the electric field is defined discretely. A Runge-Kutta scheme has been chosen to solve for particle trajectories. The scheme showing the full calculation for each time step is shown in figure 2.2.

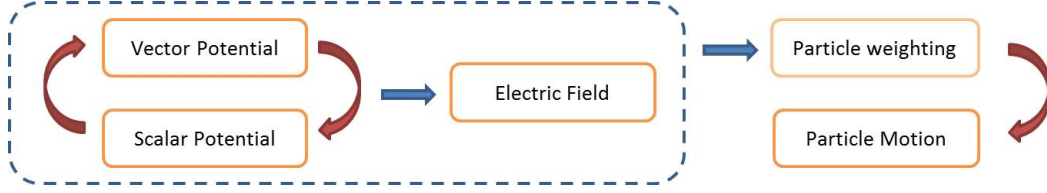


Figure 2.2: Diagram representing the update procedure into the program. Wave equations are updated one from the other. Once updated, the electric field and particle movement are calculated. A single iteration requires the calculation of a few possible trajectories, from which the final approximation is obtained.

Initial conditions for particles

At the beginning of every simulation, the spatial domain is filled/populated with a plasma in stationary state, coupled consistently with its background properties. Typically, loaded test particles are distributed according to some given space dependent density function. Such function defines a weighting factor at every position, proportional to the relative probability of finding a particle at that particular location. In the homogeneous case, for example, initial positions are assigned randomly, the chance of being located at a specific place is the same as any other place.

In phase space, distributions are generally loaded as maxwellians characterized by some known energy through the thermal velocity $v_t = \sqrt{2k_B T/m}$

$$f_M(v) = \frac{e^{-(v/v_t)^2}}{(\sqrt{\pi}v_t)^3} \quad (2.77)$$

Initial velocities are assigned by associating random numbers to the cumulative distribution function [*Birdsall and Langdon, 2005*]

$$R = \frac{\int_{-\infty}^v d\mathbf{v}' f(v')}{\int_{-\infty}^{\infty} d\mathbf{v}' f(v')} \quad (2.78)$$

Particle velocities are given in terms of components parallel and perpendicular to the background magnetic field, as suggested by the cylindrical geometry of the system. The condition of normalization is expressed as

$$\int_0^{2\pi} d\phi \int_0^{\infty} dv_{\perp} v_{\perp} \int_{-\infty}^{\infty} dv_{\parallel} f(v_{\parallel}, v_{\perp}) = 1 \quad (2.79)$$

Inversion formulas for the velocity components are obtained in terms of random

numbers R and R' [*Box and Muller, 1958*] [*Birdsall and Langdon, 2005*]

$$v_{\parallel} = v_t \sqrt{-\ln(R)} \cos(2\pi R') \quad (2.80)$$

$$v_{\perp} = v_t \sqrt{-\ln(R)} \quad (2.81)$$

For a sufficiently large number of samples, total averages tested against the first few moments might be useful for validation purposes. These are tabulated in 2.1

Table 2.1: Averages and rms predictions for a maxwellian distribution

	mean value	rms value
v_{\parallel}	0	$v_t^2/2$
$ v_{\parallel} $	$v_t/\sqrt{\pi}$	$v_t^2/2$
v_{\perp}	$\sqrt{\pi}v_t$	v_t^2
v	$\sqrt{8/\pi}v_t$	$3v_t^2/2$

Boundary particle conditions

Boundaries in the code are meant to be the ends of a finite window that is the plasma region of interest; the background plasma is supposed to extend beyond these boundaries with no modification of its properties, which means that, under stationary conditions, the flux of particles that crosses the boundary in both directions should be statistically identical to the fluxes of particle crossing any other point inside the computational domain. Periodic boundary conditions may be suitable here for a number of cases if the background properties are symmetrical at both boundaries. The simulations, however, need a more inclusive treatment, since we are considering traveling waves accelerating particles in a nonsymmetrical way, and different background conditions at each boundary. Instead of periodic conditions at the boundaries, leaving particles are simply discarded, and incoming plasma is treated as having the same distribution as the plasma initially present in the simulation domain. The effect of particle advection through the boundaries is simulated by injecting particles at every time step, according to an estimation of the flux $vf(v)$.

Flux velocities are again generated by integrating the cumulative moment and by assigning the result to a random variable. Velocities for incoming particles at

the boundaries are such that

$$v = v_t \sqrt{-\ln(1-R)} \quad (2.82)$$

The number N_B of particles to be injected at each iteration corresponds to half the particle density at the boundary n_B times the distance traveled by a particle with velocity equal to the average velocity in one time iteration

$$N_B = \frac{1}{2} n_B \langle v \rangle \Delta t \quad (2.83)$$

2.4 Scaling of physical quantities

When performing numerical calculations, it is useful to introduce a normalization for physical quantities. For example, when dealing with electrons, it is unwise to challenge the computers floating point capacity by expressing a single particles charge in Coulombs. Instead, charges are expressed as multiples of the fundamental unit of charge, which is easy to implement and furthermore makes the numerical results more understandable.

Earth's radius is chosen as a convenient normalization for the spatial domain. Real distances are expressed as $s = R_e s_n$, with s_n being the simulation variable. Avoiding any scaling in time, note that the velocity inherits the same scaling:

$$\begin{aligned} v &= \frac{dS}{dt} = \frac{d(R_e s_n)}{dt} \\ &= R_e \frac{ds_n}{dt} \\ &= R_e v_n \end{aligned} \quad (2.84)$$

Obviously, the same applies for the acceleration. The other important aspect that is revealed through normalization is how the scale factor affects variation with respect to distance. This can be seen on using the chain rule:

$$\frac{d}{ds} = \frac{ds_n}{ds} \frac{d}{ds_n} = \frac{1}{R_e} \frac{d}{ds_n} \quad (2.85)$$

In the plasmas context, elementary charge and electron mass provide a rather natural normalization for mass and charge ($q = q_n e$, $m = m_n m_e$), respectively.

To see how normalization is introduced, consider the magnetic force term in

(2.11) and the normalization factor that is consistent with magnetic induction

$$B = \frac{ma}{qv} = B_n \frac{m_e R_e}{e R_e} \quad (2.86)$$

With this, we can relate the numerical value for the gradient of the magnetic field with the real value

$$\frac{dB}{ds} = \frac{m_e}{e R_e} \frac{dB_n}{ds_n} \quad (2.87)$$

Scale factors for physical quantities are summarized in table 2.2

Table 2.2: Scaling factors for physical quantities

distance/velocity/acceleration (m)	$S = R_e S_n = 6.37 \times 10^6 S_n$
mass (kg)	$m = m_e m_n = 3.11 \times 10^{-31} m_n$
charge (C)	$q = e q_n = 1.602 \times 10^{-19} q_n$
magnetic field (T)	$B = \frac{m_e}{e} B_n = 5.685629577 \times 10^{-12} B_n$
magnetic moment (m ² A)	$\mu = R_e^2 e \mu_n = 6.521563158 \times 10^{-6} \mu_n$
electric field (V/m)	$E = \frac{R_e m_e}{e} E_n = 3.62743167 \times 10^{-5} E_n$
temperature/electric potential (eV)	$T = \frac{m_e R_e^2}{e} T_n = 231.4301406 T_n$
magnetic permeability (Tm/A)	$\mu_0 = \frac{m_e R_e}{e^2} \mu_{0n} = 2.264065012 \times 10^{14} \mu_{0n}$

Chapter 3

Code tests

The test-particle and wave models described in the previous chapter require validation, and this is the objective of the test cases that are presented in this chapter. The purpose of each test problem is described and corresponding results are reported and discussed. The programs have been tested in four aspects: (1) to ensure that the test-particle Algorithm accurately reproduces particle dynamics, (2) to obtain estimates of how faithfully wave propagation behaves under ideal and non-ideal numerical conditions, (3) to corroborate the qualitative properties expected of numerical waves propagating into an inhomogeneous plasma domain, and (4) to attempt to reproduce some physical features already published elsewhere (see for example *Kletzing* [1994] and/or *Watt et al.* [2004]) using different Algorithms for IAWs and wave-particle interactions.

For the first three cases, the spatial domain has been chosen to have a length of nine Earth radii, and an equatorial magnetic field strength equal to that of an $L = 4$ dipole field line at the equator. The loss cone angle is approximately 5.34° at the equator, and we take its intensity in SI units to fit the given expression (2.74)

$$B(s) = 4.859 \times 10^{-7}(1 + 1.386 \times 10^{-13} s^2) \quad (3.1)$$

3.1 Test 1: Dynamics of a single particle

A single particle is initially located at the origin of the domain with a certain known initial kinetic energy and pitch angle. In absence of electric fields, the mirror force is the only one affecting the particle. Subsequent gyromotion resembles simple

harmonic motion

$$\frac{dv_{\parallel}}{dt} = -\frac{2\mu_s B_0}{m_s s_0^2} s = -D^2 s \quad (3.2)$$

where $D^2 = 2\mu_s B_0 / (m_s s_0^2)$. The definition $v_{\parallel} = ds/dt$ can be used to eliminate the temporal dependence

$$\frac{\frac{ds}{dt}}{\frac{dv_{\parallel}}{dt}} = \frac{v_{\parallel}}{-D^2 s} \quad (3.3)$$

The analytical solutions of the previous equation correspond to trajectories that are ellipses in phase-space

$$v_{\parallel}^2 + (Ds)^2 = v_0^2 \quad (3.4)$$

A particle moving in phase space eventually reaches the turning point of the magnetic mirror, at which $v_{\parallel} = 0$; from (3.4) two values of the spatial coordinate at this point are obtained

$$s_m = \pm \frac{v_0}{D} = \pm \frac{s_0^2}{\tan(\alpha_{eq})} \quad (3.5)$$

To solve for the position as a function of time, return to the definition $v_{\parallel} = ds/dt$. Substituting the solution of (3.4) for v_{\parallel} and integrating leads to the following result

$$t(s) = \frac{1}{D} \arctan \left(\frac{Ds}{\sqrt{v_0^2 - (Ds)^2}} \right) \quad (3.6)$$

Evaluation of (3.6) at the mirror point allows calculation of the bounce period

$$\tau_b = 4t(s_m) = \frac{2\pi}{D} \quad (3.7)$$

The trajectory as a function of time is obtained by solving (3.6) for s

$$s(t) = \frac{v_0}{D} \sin(Dt) \quad (3.8)$$

3.1.1 Obtained results

Graphs of phase-space (3.1(a)) and position as a function of time (3.1(b)) are shown in figure (3.1), created from data obtained from the code. The observed behaviour is as expected from the considerations stated previously, the phase-space diagram

shows an ellipse not deformed after the particle has performed several bounces along the computational domain.

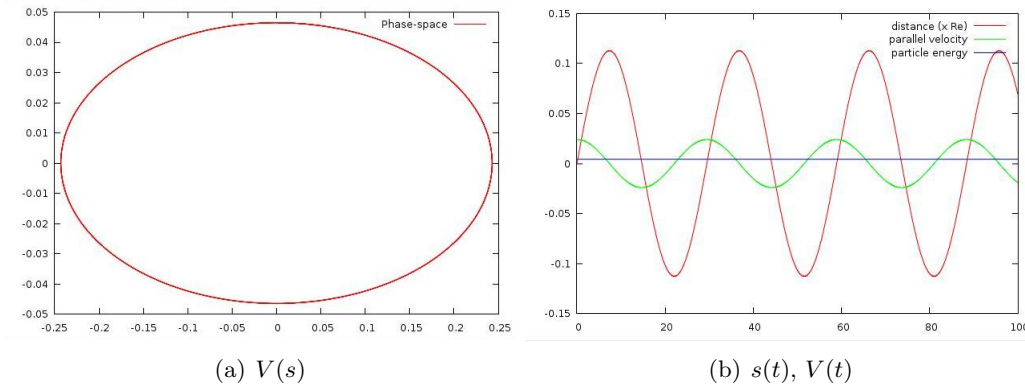


Figure 3.1: Phase space and temporal behaviour for a particle embedded in a quadratic magnetic field.

The program was run several times for several energies and initial pitch angles, and for each run the bounce period and the returning point were obtained from the numerical output.

Table 3.1 shows a comparison between the expected and simulation results. The numerical results are exact up to the third significant figure, which means that we have differences of less than 1% with respect to the analytical values. These difference includes not only errors from floating point arithmetic and from the numerical method; additionally, the values shown do not exactly correspond to one bounce period because of the time discretization used in the Algorithm.

Table 3.1: Expected (τ_E) and Numerical (τ_N) bounce periods in seconds, after the first bounce, at several pitch angles and energies for one particle.

Particle energy (eV)	1		10		100		1000	
	τ_E	τ_N	τ_E	τ_N	τ_E	τ_N	τ_E	τ_N
$\alpha_{eq} (^{\circ})$								
15	109.932	109.94	34.763	34.77	10.993	10.994	3.476	3.475
30	56.905	56.91	17.995	18	5.690	5.691	1.799	1.8
45	40.238	40.24	12.724	12.73	4.024	4.024	1.272	1.275
60	32.854	32.86	10.389	10.39	3.285	3.286	1.039	1.039
75	29.456	29.46	9.315	9.32	2.946	2.946	0.931	0.932

Table 3.2 compares maximum distance from the center (equator) to the mirror

point reached by the particle. In this case differences occur after the fifth significant number, and as in the previous case, besides the unavoidable errors due to the numerical approximation and floating point arithmetic, the values shown do not strictly correspond to the mirror point, but to the best approximation obtained for the spatial discretization given.

Table 3.2: Expected (E) and first reached Numerical (N) turning points for a particle with energy 1000 eV at several pitch angles.

Pitch angle ($^{\circ}$)	$s_{mE} (R_E)$	$s_{mN} (R_E)$
15	1.571055098	1.5710551
30	0.729129208	0.72912919
45	0.420962945	0.42096294
60	0.243043069	0.24304298
75	0.112796681	0.11279662

3.2 Test 2: Wave propagation in a uniform medium

Previously, an expression relating wave propagation to the physical (homogeneous) medium (equation 2.57) was given, along with a condition under which numerical waves exactly reproduce the propagation features of analytical waves (equation 2.66). It is expected that some discrepancy in the phase velocity of the numerical wave will occur whenever the space and time discretization do not match the ideal condition. It is then necessary to quantify these discrepancies in order to find an acceptable tolerance level which ensures that numerical wave propagation is appropriately *accurate*.

In order to determine how good or bad numerical wave propagation is, the wave program was run several times, varying the value of the parameter β ; this implies that we are observing numerical wave propagation in different homogeneous mediums for the same space and time discretization. Despite nonideal conditions, changes in the parameters were such that the predicted velocity was always below the limit velocity allowed by the Courant condition: $v_{\parallel} \leq V_L = \Delta s / \Delta t$. Phase velocities of the simulated waves were measured and compared to theoretical values.

Table 3.4 compares the phase velocity with nonideal numerical conditions to the ideal case. Numerical velocities show very little difference with expected velocities for the range $[V_L/20, V_L]$.

Table 3.3: Constant numerical parameters used in all simulations

Number of iterations	500
Space domain total length (R_E)	9
Wave Amplitude Φ_0 (num)	.5
Space discretization unit ds (R_E)	.0045
Time discretization unit dt (s)	.0045
Phase velocity limit V_L (R_E/s)	1
αc^2 ($(R_E/s)^2$)	1
Wave period (s)	1

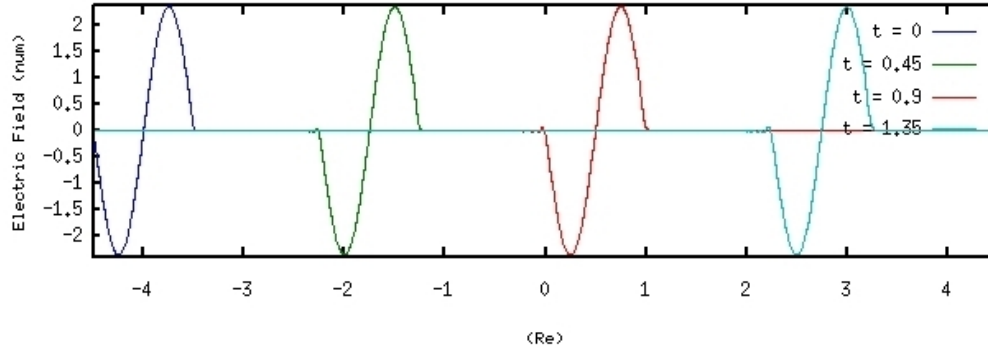


Figure 3.2: Waveform for propagation in homogeneous media at different times.

3.3 Test 3: Wave propagation on a nonuniform medium

In the previous subsection, we considered wave propagation in uniform media. Along Earth's magnetospheric field lines, however, plasma density and magnetic field change with the local value of $v_A(B(s), \rho(s))$

3.3.1 Expected behaviour

For the nonuniform case a few qualitative characteristics of the propagating wave were compared to theoretical predictions. Let us write the analytic dispersion equation (2.57) in terms of the Alfvén velocity; substitute $\alpha(s)$ from equation (2.50) and $\beta(s)$ from (2.70) to obtain

$$v_{phase} = \frac{V_{AC}}{(V_A^2 + c^2) \left(\sqrt{1 + \left(\frac{2\pi}{\lambda_I} \right)^2 \frac{m_i m_e}{B_I} \frac{V_A(s)^2}{B(s)}} \right)} \quad (3.9)$$

Table 3.4: Expected ($V_{\parallel E}$) and Numerical ($V_{\parallel N}$) phase velocities for different β parameters

β	Wavelength (R_E)	$V_{\parallel E}$ (R_E/s)	$V_{\parallel N}$ (R_E/s)	$V_L/V_{\parallel E}$
1	2.	1.	.998	1
16	.5	.25	.25	4
64	.25	.125	.124	8
144	.1667	.0833	.084	12
256	.125	.0625	.062	16
400	.1	.05	.05	20

Here B_I and λ_I refer to typical values of magnetic field magnitude and perpendicular length scale at the ionosphere. Notice that the mass dependence in the denominator, suggest propagation with phase velocity very close to the Alfvén velocity for nonrelativistic waves. Other observable characteristic refers to the wavelength of the wave. Recall from elementary physics that $v_{\parallel} = \lambda\nu$, which means the wavelength is proportional to the phase velocity for a given frequency.

3.3.2 Simulation output

Previous considerations were tested with the wave algorithm. A sequence of pictures taken successively after a fixed time interval is included in figure 3.3. The green line represents the Alfvén velocity as function of position. It can be seen that the wave barely moves until half-way through the simulation, and the wavelength during this interval changes very little. Thereafter, both the phase velocity and the wavelength have a significant increase, which coincides with the fact that the wave now moves into a region where the Alfvén velocity is significantly increasing.

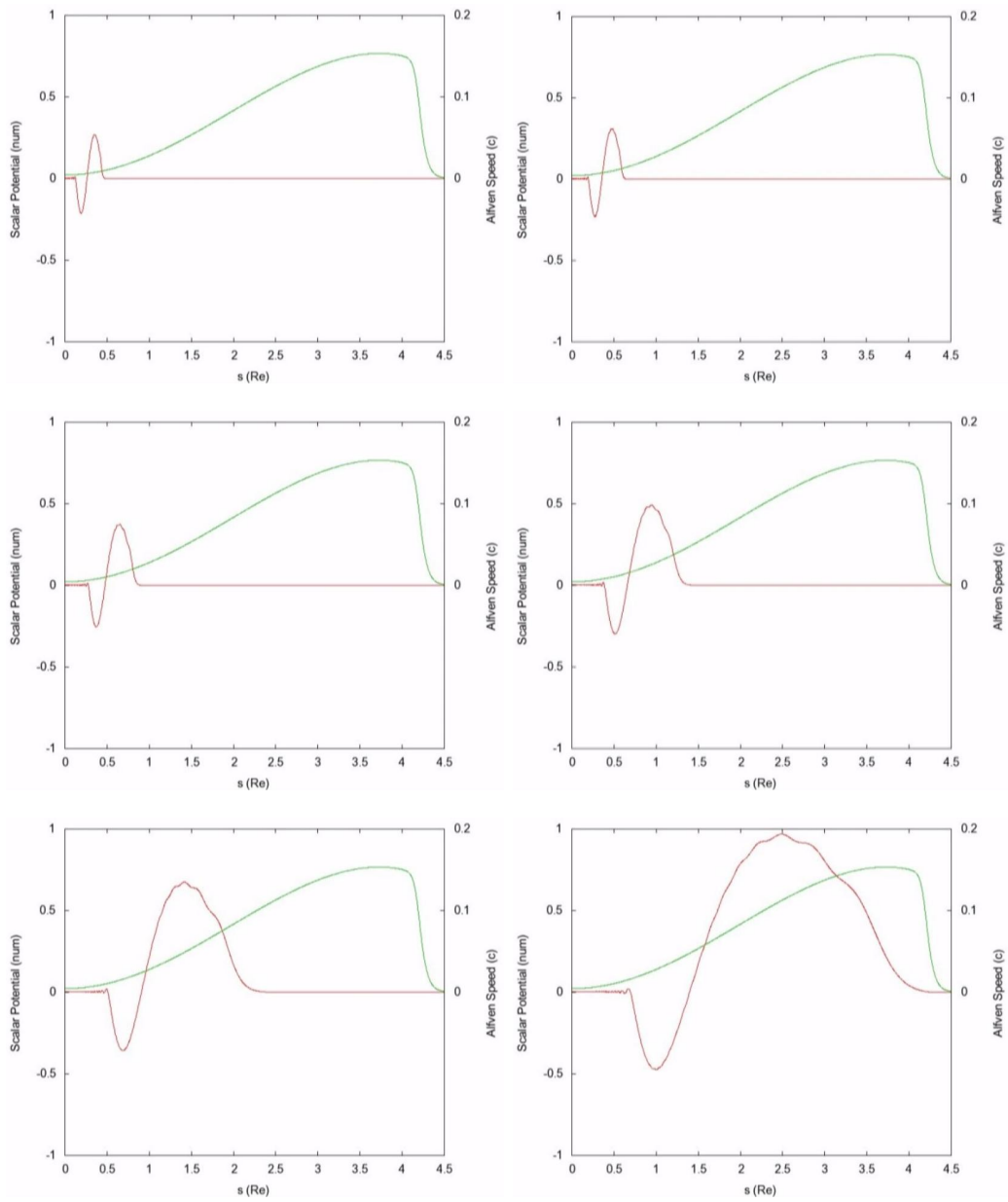


Figure 3.3: Snapshots of wave propagation into an inhomogeneous medium. Alfven velocity profile is also shown

3.4 Test 4: Wave - particle interaction in homogeneous medium

According to the theory of IAWs, particle acceleration depends, through the parallel electric field, on the local gradient of the potential with distance (2.67). For the case of a uniform background magnetic field, equation (2.76) yields

$$a = \frac{e}{m} \left(1 - \frac{1}{\beta}\right) \frac{\partial \phi}{\partial s} \quad (3.10)$$

According to definition (2.51), $\beta > 1$, so positive acceleration for electrons is expected whenever $\frac{\partial \phi}{\partial s} > 0$, and deceleration in the opposite case. The total time a particle is under the influence of a given polarization of the electric field determines the amount of acceleration it undergoes; then particles with velocities close to the phase velocity of the wave travel with it, and at the same time are accelerated by it for the longest time. These so-called resonant particles are expected to gain the largest amount of energy through interaction with IAWs.

A simulation with an initially Maxwellian electron population embedded in a uniform magnetic field and an incoming sinusoidal wave pulse was performed to evaluate the particle acceleration produced by IAWs. Initial simulation parameters are similar to those used in *Watt et al.* [2004], and these are shown in table (3.5)

Table 3.5: Numerical parameters for a simulation of IAW propagation into a Maxwellian plasma in a uniform magnetic field

Total domain length (R_e)	5
Δs (R_e)	0.02
Δt (s)	0.12
k_{\perp} (m^{-1})	2.63×10^{-3}
Background magnetic field (nT)	6500
T_e (eV)	10
v_{ph} (R_e/s)	~ 1.5
ϕ_0 (V)	200

A single pulse $\phi(s, t) = \phi_0 \cos(ks - \omega t)$ is injected through one of the borders of the computational domain. The period and wavelength were chosen so that the wave moves according to the condition $k_{\parallel} \Delta s = \omega \Delta t$. Each snapshot in figure 3.4 shows the parallel phase distribution (left) and the wave electric field profile (right) obtained every 50 iterations. Although in the simulation the wave is incorporated as if it was initially outside the simulation domain, time $t = 0$ s has been chosen to

be the instant just after the wave is fully inside the space domain, which explain why the electron distribution seems as if it had been disturbed instantaneously in figure 3.4(a).

Results of similar simulations have been published by *Kletzing* [1994] and *Watt et al.* [2004]. In the first of these publications, two acceleration processes were identified, which can also be appreciated here: (1) there is acceleration of the whole plasma at some location in the neighbourhood of the electric field minima, evident in the figure as a lateral displacement of the bulk distribution towards higher parallel velocities. This kind of acceleration has been interpreted in *Watt et al.* [2004] as the electron's movement required to carry the current necessary for wave propagation, (2) a much stronger acceleration of the small fraction of the electrons initially moving at velocities slightly lower than the phase velocity of the pulse. These *resonant* particles are eventually reached and trapped by the wave, experiencing the effect of the negative electric field for the longest time, and while trapped, being accelerated in the direction of wave propagation. The electric field energizes the electrons, allowing them to escape and form a beam-like structure in front of the wave. A maximum velocity for resonant electrons was pointed out by *Kletzing* [1994] to be $\sim 2v_{ph}$ with respect to an observer at rest. In the simulation presented here, it is apparent that the maximum velocity is close to, but less than this limit. It seems that there are very few resonant particles in this case, their density not being high enough as to appear noticeably on the figure. *Watt et al.* [2004] reported also electron acceleration in the direction opposite to the electric field, this effect is not evident in our results, possibly also due to the relatively high velocity of the wave relative to the particles; particles with initially negative velocities, which are the ones that would resonate with the positive electric field, do not spend enough time in the presence of the electric field as to obtain the necessary energy to be accelerated noticeably.

Watt et al. [2004] used a self-consistent formulation to analyze the same problem. There, features regarding electron acceleration and wave damping were found. An example of particle-wave feedback found in their simulations, is the parallel component of the current carried by the wave, which changes in time due to the perturbation of the electron distributions. This and other effects due to particle-wave interactions are not expected to appear in our simulation since our code is not self-consistent.

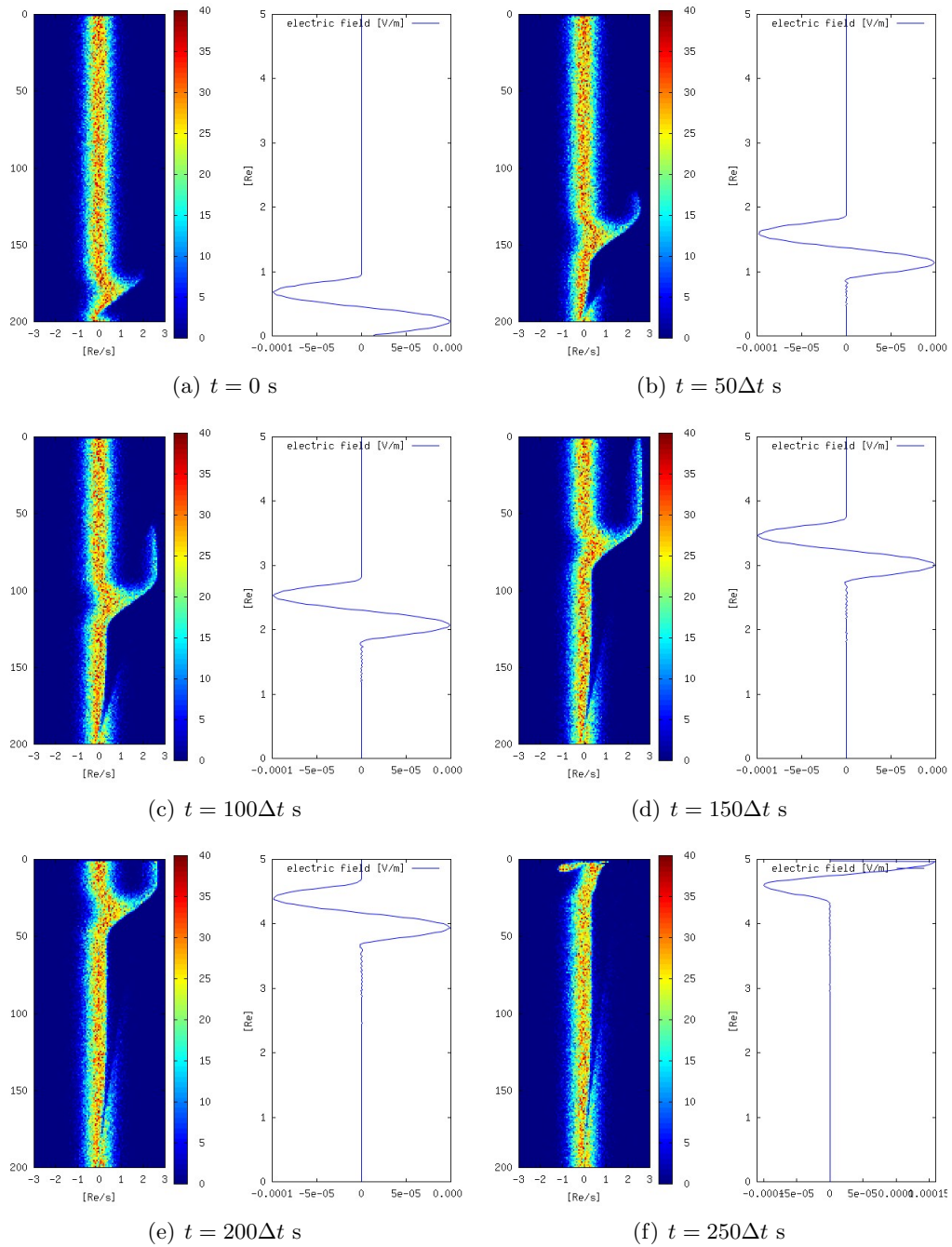


Figure 3.4: *left* A representation of parallel velocity density and *right* parallel electric field along the spatial domain (position along domain is represented by the vertical axis)

Chapter 4

Results

The ultimate goal and motivation for the creation of our test particle code, is the study of the effect of inertial Alfvén waves upon plasmas that resemble the plasma present in the auroral cavity, where the Auroral Kilometric Radiation is generated and emitted. Upon the passing of an electromagnetic pulse through plasma in an initial stationary state, we can observe variations on the distribution of particles. More specifically, we want to identify possible instabilities associated with plasma interaction with IAWs.

4.1 Background plasma properties

As a first attempt to do some research work, we keep using the background parameters related to the $L = 4$ magnetic field line. A few changes are needed, though, with respect to the background properties implemented in our test runs: the magnetic bottle configuration used before was a good start to measure individual particles dynamics and to observe the evolution of wave pulses as they traveled to a regions where the Alfvén velocity had a significant gradient. It is not, however, that convenient when it comes to study particle acceleration, because due to the relative fast grow of the magnetic intensity in most of the spatial domain, the Alfvén profile also grows at what it would correspond to low latitudes. When trying to perform simulations, this rapid grow makes incoming waves to increase their wavelength to scales of the order of the whole spatial domain length, and the amplified electric field would practically wipe out the resonant particles by accelerating them to very high velocities, so they leave the computational domain in very little time. In a self consistent treatment, such effect is not expected since acceleration of particles produces damping in the waves. To sort out this situation,

a dipolar form for the magnetic field is sampled discretely, and its value at an arbitrary location is linearly interpolated from the two closest points where it is defined. So we assume the magnetic field to have a dipolar form [*Baumjohann and Treumann, 1997*]

$$B(s) = \frac{B_E}{L^3} \frac{\sqrt{1 + 3 \sin^2 \lambda(s)}}{\cos^6 \lambda(s)} \quad (4.1)$$

The density variation in space has been also redefined to a simpler form. In our case, the atmosphere density is pictured to be the superposition of a constant background contribution of magnetospheric plasma composed mainly by hydrogen ions and electrons, and plasma of ionospheric origin for which the source comes from oxygen ionization, and its density changes according to the hydrostatic approximation

$$n(s) = n_H + n_O e^{\frac{s-s_i}{h_0}} \quad (4.2)$$

s_i denote the location of the intersection of the ionospheric border with the magnetic field line. This friendlier version allows simplifying the work of finding the necessary conditions to make the density distribution consistent with the state of equilibrium.

4.2 Consistency of the equilibrium distribution

As also was pointed out before, our code in its formulation is concerned with a limited amount of the real physics, namely, the one related to wave-particle interactions only. Therefore, many physical effects are not reproduced and must be manually programmed in order for them to appear into the simulations. One of such important effects is the initial state of the plasma, which must be artificially made consistent in its stationary state in order to properly observe the influence of waves.

In order to carry on with the simulation, we want the plasma to be in its equilibrium state at the moment of launching the wave pulse, so any variations in the distribution can be attributable to the wave interaction and its influence can be measured as accurately as possible. A Maxwell-Boltzmann distribution has been chosen as our initial equilibrium distribution, which in its normalized form is

defined as

$$f_M(v) = \frac{e^{(v/v_{th})^2}}{(\sqrt{\pi}v_{th})^3} \quad (4.3)$$

where $v_{th} = \sqrt{2k_B T/m}$ is the thermal speed, a parameter related to the plasma temperature or internal energy.

We are still faced with the problem of making the stationary distribution to match the density profile (4.2) consistently. To mimic the effect of gravity keeping the cold plasma close the ionospheric border, we imagine the spatial domain to be embedded in a conservative electrostatic field $U(\mathbf{r}) = q\phi(\mathbf{r})$

$$\mathbf{F}(\mathbf{r}) = -\nabla U(\mathbf{r}) \quad (4.4)$$

which should include some position dependence into the distribution function. Then we expect the equilibrium distribution to have the form

$$f(\mathbf{r}, v) = f_M(v)\psi(\mathbf{r}) \quad (4.5)$$

Following [Bittencourt \[2005\]](#), the function $\psi(\mathbf{r})$ is found by neglecting the term of temporal variation in the Vlasov equation, a step valid under the assumption of equilibrium. Then we are left with

$$\mathbf{v} \cdot \nabla [f_M(v)\psi(\mathbf{r})] - \left[\frac{\nabla U(\mathbf{r})}{m} \right] \cdot \nabla_{\mathbf{v}} [f_M(v)\psi(\mathbf{r})] = 0 \quad (4.6)$$

Expanding this expression and dividing by $f(\mathbf{r}, v)$, it is easy to get

$$\mathbf{v} \cdot \nabla \left[\ln \psi(\mathbf{r}) + \frac{U(\mathbf{r})}{k_B T} \right] = 0 \quad (4.7)$$

with solution

$$\psi(\mathbf{r}) = e^{-U(\mathbf{r})/(k_B T)} \quad (4.8)$$

In summary, the number density is equal to the case of no force field, modulated by a position dependent factor involving the electrostatic potential

$$n(\mathbf{r}) = e^{-(q\phi(\mathbf{r}))/(k_B T)} \int d\mathbf{v} f_M(v) \quad (4.9)$$

4.2.1 Determination of the electrostatic potential

According to the logic of the last subsection, plus the description of the chosen variation of density provided in (4.2), we can express the distribution function as an addition of two Maxwellians with temperatures T_c (cold) and T_w (warm), each modulated by the presence of the scalar potential [Tikhonchuk and Rankin, 2002]

$$f(v) = \frac{n_c}{(\sqrt{\pi}v_{thc})^3} e^{-\omega_c/T_c} + \frac{n_w}{(\sqrt{\pi}v_{thw})^3} e^{-\omega_w/T_w} \quad (4.10)$$

where $\omega_{c/w} = (1/2mv^2 - e\psi(s))$. Also here we have redefined the temperature as $T = k_B T$. The integrated density corresponds to

$$n(s) = n_c e^{e\psi(s)/T_c} + n_w e^{e\psi(s)/T_w} \quad (4.11)$$

and the temperature is given by

$$n(s)T(s) = n_c T_c e^{e\psi(s)/T_c} + n_w T_w e^{e\psi(s)/T_w} \quad (4.12)$$

The unknown quantities n_c and n_w can be found in terms of the provided densities at the magnetospheric and ionospheric limits, n_H and n_O respectively. By choosing $\psi(s_i) = \psi_i$ and $\psi(0) = 0$, we have

$$\begin{pmatrix} 1 & e^{-s_i/h_0} \\ 1 & 1 \end{pmatrix} \begin{pmatrix} n_{H_2} \\ n_{O_2} \end{pmatrix} = \begin{pmatrix} 1 & 1 \\ e^{e\psi_i/T_c} & e^{e\psi_i/T_w} \end{pmatrix} \begin{pmatrix} n_c \\ n_w \end{pmatrix} \quad (4.13)$$

Then n_c and n_w are given by

$$\begin{pmatrix} n_c \\ n_w \end{pmatrix} = \frac{1}{e^{e\psi_i/T_w} - e^{e\psi_i/T_c}} \begin{pmatrix} e^{(e\psi_i/T_w)} - 1 & e^{(e\psi_i/T_w - s_i/h_0)} - 1 \\ 1 - e^{(e\psi_i/T_c)} & 1 - e^{(e\psi_i/T_c - s_i/h_0)} \end{pmatrix} \begin{pmatrix} n_{H_2} \\ n_{O_2} \end{pmatrix} \quad (4.14)$$

Not every value of ψ_i is valid. From the fact that both n_c and n_w are positive numbers, the following condition arises

$$T_c \ln \left(\frac{n_{H_2} + n_{O_2}}{n_{H_2} + n_{O_2} e^{-s_i/h_0}} \right) \leq e\psi_i \leq T_w \ln \left(\frac{n_{H_2} + n_{O_2}}{n_{H_2} + n_{O_2} e^{-s_i/h_0}} \right) \quad (4.15)$$

whenever the quantity $D = e^{e\psi_i/T_w} - e^{e\psi_i/T_c} < 0$, it can also be shown that there is no solution for the case $D > 0$, which is consistent with the fact that the electrostatic potential can hold the electron distribution for only positive potentials with respect to the equator. The associated electric field pushes the electrons

towards the ionospheric border, which is consistent with the given particle density variation with position.

Notice that, by using the boundaries to relate the cold and warm background contributions, we have introduced another unknown parameter, the potential at the ionospheric border ψ_i . Alternatively, we can argue that the warm plasma is constituted by magnetospheric electrons basically

$$n_w \simeq n_{H_2} \quad (4.16)$$

This condition restricts the range of parameters to $n_w \gg n_c$, as can be noticed by evaluating (4.11) at the equator. From the same boundary, n_c is found to be

$$n_c = n_{O_2} e^{-s_i/h_0} \quad (4.17)$$

so we end up with an expression independent of ψ_i

$$n(s) = n_{H_2} e^{e\psi(s)/T_w} + n_{O_2} e^{-s_i/h_0} e^{e\psi(s)/T_c} \quad (4.18)$$

Numerical solution of the electrostatic potential

It is not possible to solve for $\psi(s)$ in (4.18) analytically. Instead, the Interval Bisection method is implemented to generate a list of discrete values for the potentials all along the magnetic field line. Once these potentials are found, it is also possible to generate a discrete temperature profile using (4.12). These profiles have been plotted in figure 4.1 as a function of the position in the spatial domain, which is approximately $4.5R_e$ long from the equator up to its intersection with the Earth surface. The known density function of position (4.2) and temperatures at the boundaries are consistent with the obtained potential.

4.3 Building up the equilibrium distribution

A significant simplification arises if both species have the same temperature. For such case, the electrostatic potential is obtained analytically from (4.11)

$$e\psi(s) = T \ln \left(\frac{n_w + n_c e^{s/h_0}}{n_w + n_c} \right) \quad (4.19)$$

In our simulation, we consider the case of both species having the same temperature. Background densities are given by (4.16) and (4.17). Some numerical parameters and a few derived properties for each species are shown in table 4.1.

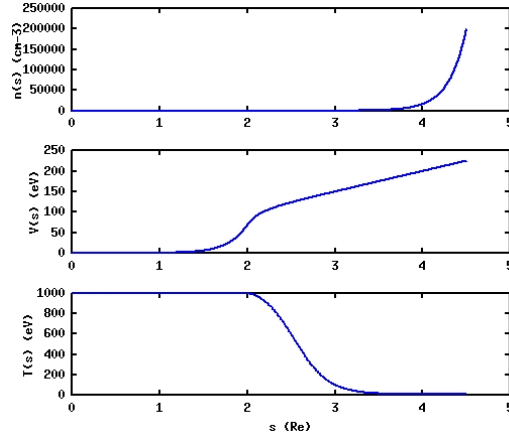
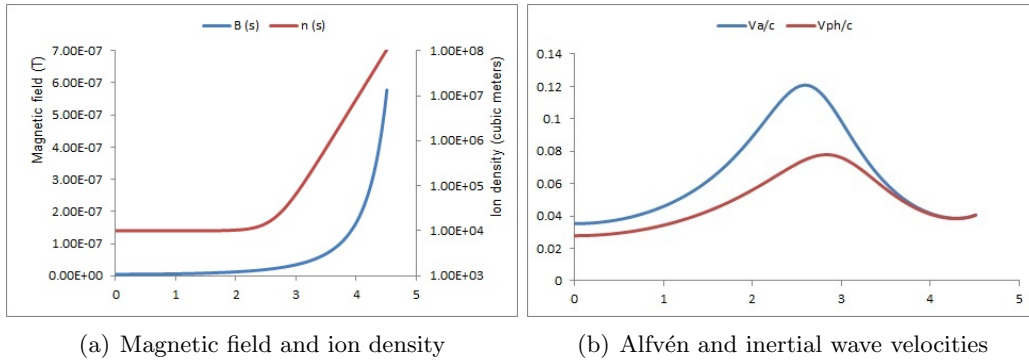


Figure 4.1: Variation of density, electrostatic potential and temperature along a section of magnetic field line. The parameters given are: $n_{H_2} = 10 \text{ cm}^{-3}$, $n_{O_2} = 2 \times 10^5 \text{ cm}^{-3}$, $T_c = 10 \text{ eV}$, $T_w = 1 \text{ keV}$, $s_i = 4.5R_e$ and $h_0 = .2R_e$

These parameters define for the simulation domain the magnetic field and ion density variations in space, which determine the properties of propagation of magnetic signals; the corresponding Alfvén speed and phase speed of shear modes are shown in figure 4.2



(a) Magnetic field and ion density

(b) Alfvén and inertial wave velocities

Figure 4.2: Background plasma properties

Particles initial positions

The total number of particles inside the spatial domain is an arbitrary parameter to the simulation. However, the ratio of cold to warm particles must be maintained numerically since it is enforced by the state of equilibrium. This relation is easily

Table 4.1: Numerical parameters defining background magnetic field and plasma density

L	4
n_{H_2} (cm ⁻³)	1
n_{O_2} (cm ⁻³)	10 ⁴
s_i (Re)	4.5
h_0 (Re)	0.2
$T_c = T_w$ (eV)	10
n_w (cm ⁻³)	1
n_c (cm ⁻³)	1.6919×10^{-6}
N_w	591052
N_c	0

found to be

$$\frac{N_w}{N_c} = \frac{n_w}{n_c} \quad (4.20)$$

as found through integration of each species density function (4.18) with respect to the position along the magnetic field line.

Numerically, loading of particles is based on the relative probability of finding a particle at a given location. Due to the exponential nature of the density profile, most of the test particles tend to pile up very close to the ionospheric border, a region not particularly interesting when it comes to observe wave-particle interactions. For this reason, it is convenient to reduce the ionospheric limit up to which particles are restricted to exist to some lower value s_x such that $0 < s_x \leq s_i$. While maintaining the numerical particle density consistent with equation (4.2) at $0 < s \leq s_x$, this allows having a comparatively higher number of particles at the regions with lower densities, which is always a desirable feature if one wishes to get decent statistics everywhere. Figure 4.3 compares the distribution of particles constructed using this procedure, with the plasma density as estimated using (4.11) and taking $s_x = 3.5Re$.

Initial phase distribution

A Maxwellian plasma of 10 eV energy was loaded according to the method described in in chapter 2. Table 4.2 compares several moments against statistical prediction (see table 2.1). The close agreement for all the calculated moments is proof that the loaded distribution indeed corresponds to a maxwellian with the specified temperature. Diagrams of the initial phase distribution are shown in

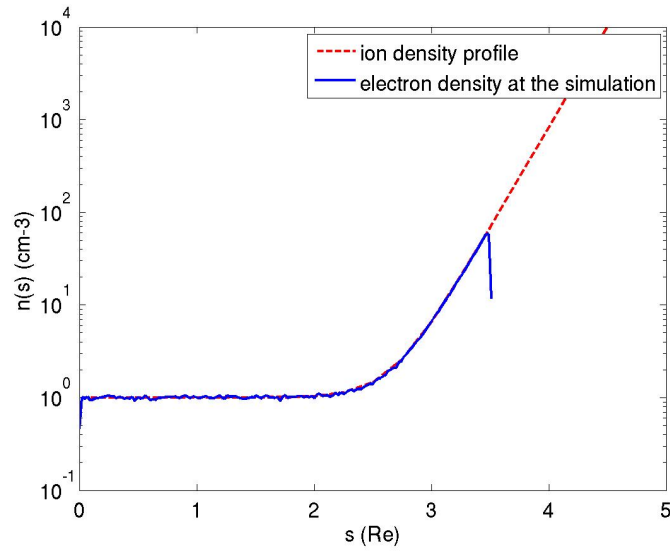


Figure 4.3: Ion density as a function of position. Initial plasma is distributed spatially in the interval $[0, 3.5Re]$

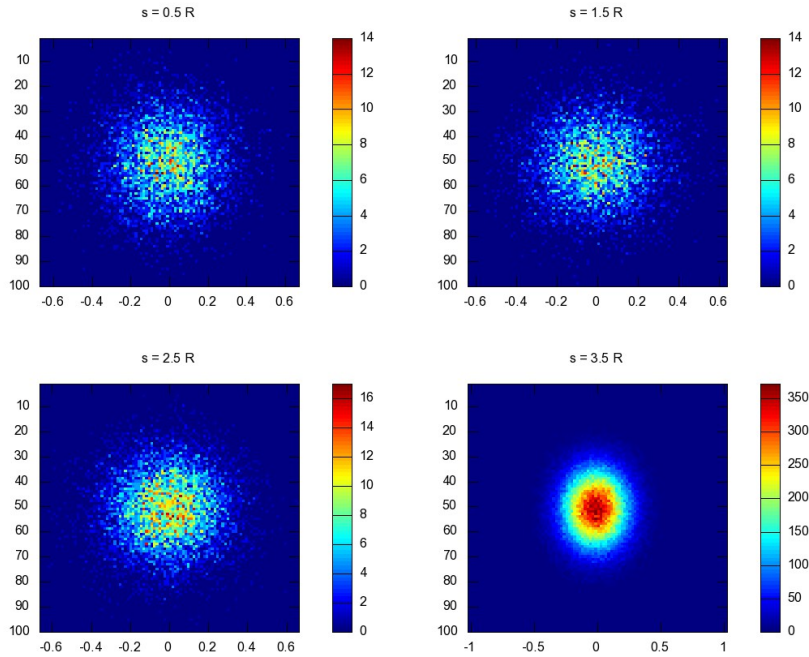


Figure 4.4: Local $(v_{\parallel}, v_{\perp})$ electron density at few different places of the simulation domain

figure 4.4 at four different locations sampling the entire spatial domain.

Table 4.2: Several typical velocities of the initial distribution of loaded particles with temperature $T = 10$ eV

	Theoretical prediction	Obtained value
$\langle v_{\parallel} \rangle (R_e/s)$	0	-1.9876×10^{-4}
$\langle v_{\parallel} \rangle (R_e/s)$	0.13561	0.13562
$\langle v_{\parallel}^2 \rangle (R_e/s)^2$	0.16996	0.17001
$\langle v_{\perp} \rangle (R_e/s)$	0.21302	0.21303
$\langle v \rangle (R_e/s)$	0.27122	0.27125
$\langle v^2 \rangle (R_e/s)^2$	0.29439	0.29443

Testing the initial state

Before introducing wave pulses into the system, it is important to evaluate how *stationary* is the loaded plasma. In our case, despite constructing the initial dynamical state of the plasma based on a theoretical formulation that predicts an state of equilibrium, simulations show that the loaded plasma is not in stationary state; the state of the distribution is strongly affected by the electrostatic and magnetic forces.

Two situations with different boundary conditions have been observed, in both cases, particles have been left to escape once they move beyond the borders of the spatial domain. In the first case, no new particles are incorporated to the simulation at the boundaries, so we do not really expect the plasma to remain stationary at the neighbouring region to the borders. In the second situation, constant particle fluxes of maxwellian plasma are injected at every time step through the boundaries, the number of injected particles is supposed to correspond to electron densities at their respective boundaries.

The sequence shown in figure 4.5 compares the time evolution of the loaded plasma to the expected ion density profile for the two cases of boundary conditions described previously. In both cases, a high fraction of the electrons initially at the ionosphere tend to move to lower latitudes. The change is much more noticeable for the simulation at which particle fluxes have been implemented. Moreover, 4.6 evidences that the maxwellian flux incorporated at the ionospheric boundary (at $s = 3.5R_e$) does not couple to conserve the initial distribution in time; it produces a large tail of particles with high antiparallel velocities and close-to-zero perpendicular velocities, possibly formed due to the action of the strong mirror force at that location, which transforms perpendicular into (anti)parallel momentum for

particles moving towards the equator; that is, however, a feature that was not properly studied here. Injection of particles at the magnetospheric boundary, on the other hand, seems to help to conserve the plasma density at low latitudes, without visibly affecting the velocity distribution at higher latitudes.

4.4 Wave-plasma interaction at an inhomogeneous media

From the previous section, it was established that the initial state of plasma is rapidly disturbed, losing its original distribution in space after very few seconds and, specifically at the ionospheric border, its velocity distribution is strongly modified almost immediately. Few seconds, however, is about the time that takes for a wave to move to sufficiently high latitudes to observe some interaction. In our simulation, a wave pulse propagates from the equator along the magnetic field line, the situation is analogous to the homogeneous case reported in section 3.4. Other than the inhomogeneous nature of the distribution of electrons and the magnetic field, and the absence of particle fluxes at the boundaries, initial parameters in this case are similar to the homogeneous case (see table 4.3)

Table 4.3: Numerical parameters for an IAW pulse into an inhomogeneous magnetic field

Total domain length (R_e)	4.5
Δs (R_e)	0.0045
Δt (s)	0.001
k_{\perp} (m^{-1})	2.63×10^{-3}
T_e (eV)	10
$v_{ph}(t = 0)$ (R_e/s)	~ 1.313
$\phi_0(s = 0)$ (V)	200

As in the homogeneous case, most of the particles at the location of the wave have higher parallel velocities than plasma in other regions, as can be seen in figure 4.7. Acceleration and deceleration of electrons are obviously associated to the negative and positive electric field sections of the pulse; an electric field antiparallel to the magnetic field forces the electrons to move in direction parallel to the magnetic field, while a positive electric field implies acceleration in the antiparallel direction. Particles inside the wave, towards the leading and at the end of the pulse, have relatively low parallel velocities, while particles with higher parallel velocities are accumulated somewhere close to the center of the pulse, some of them under the

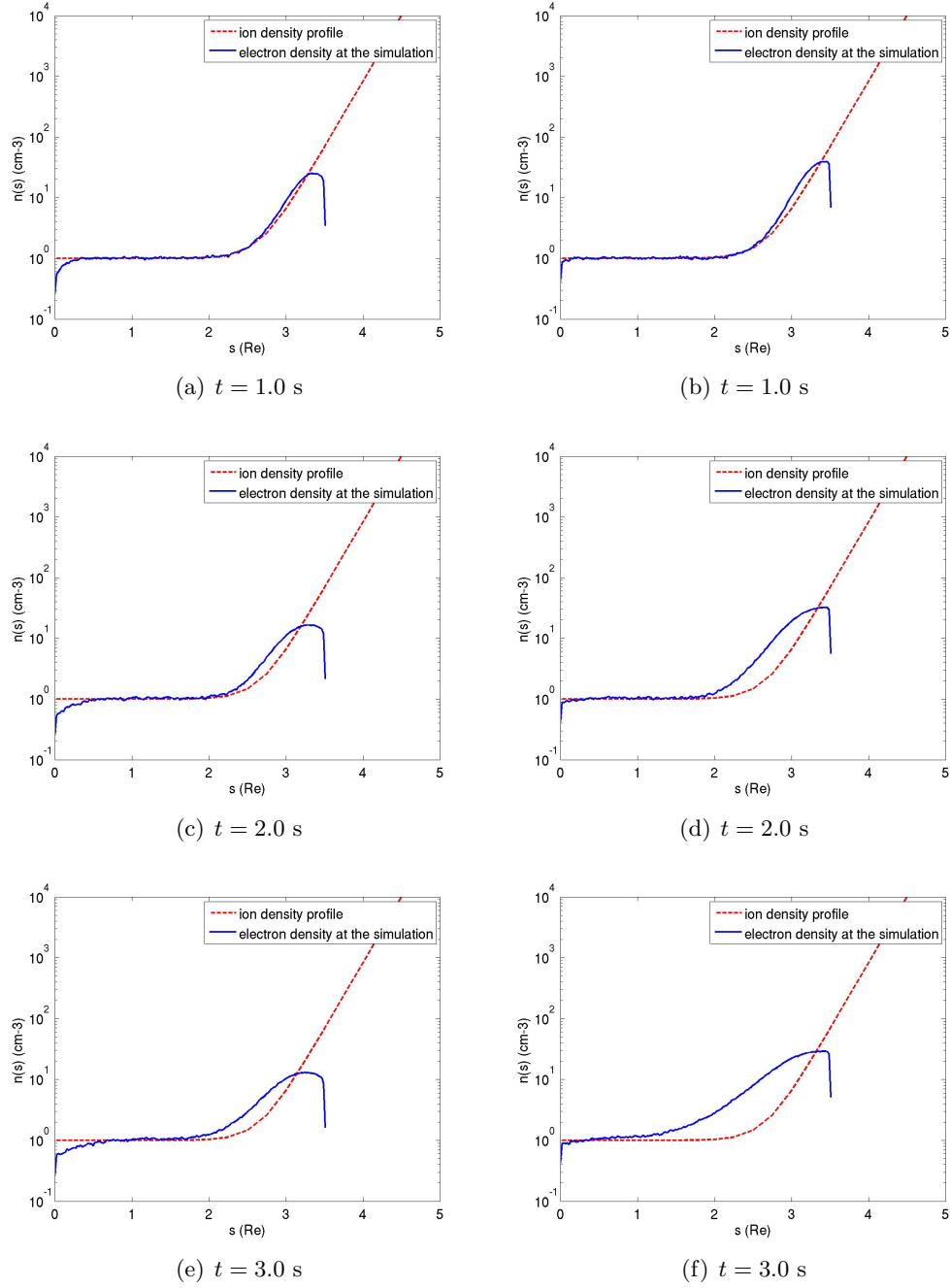
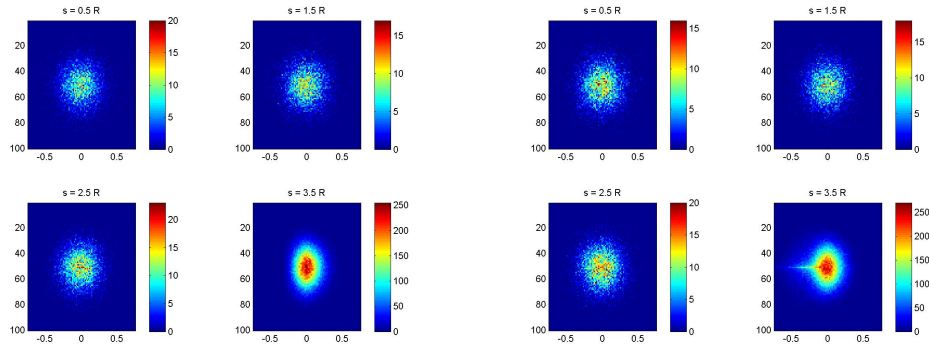
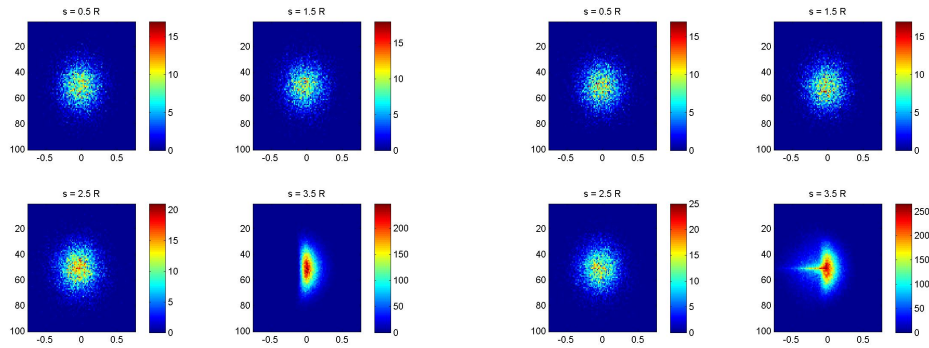


Figure 4.5: Time evolution of electron density as a function of position. (*left*) No new particles are introduced. (*right*) New particles are injected through boundaries at every time step.



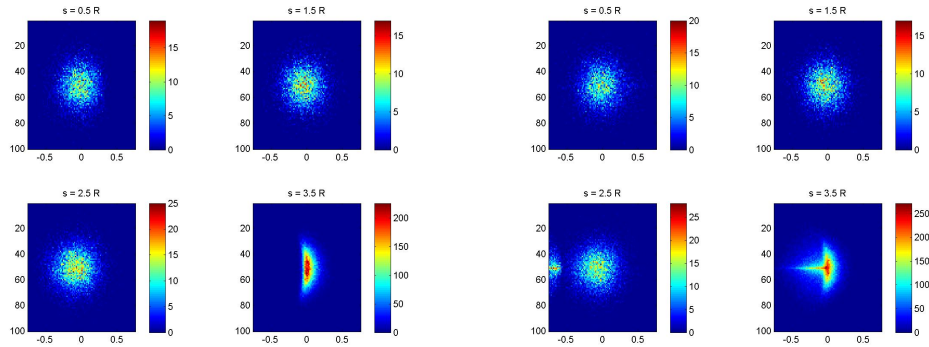
(a) $t = 0.3$ s

(b) $t = 0.3$ s



(c) $t = 0.9$ s

(d) $t = 0.9$ s



(e) $t = 1.5$ s

(f) $t = 1.5$ s

Figure 4.6: Time evolution of electron density in phase. (*left*) No new particles are introduced. (*right*) New particles are injected through boundaries at every time step.

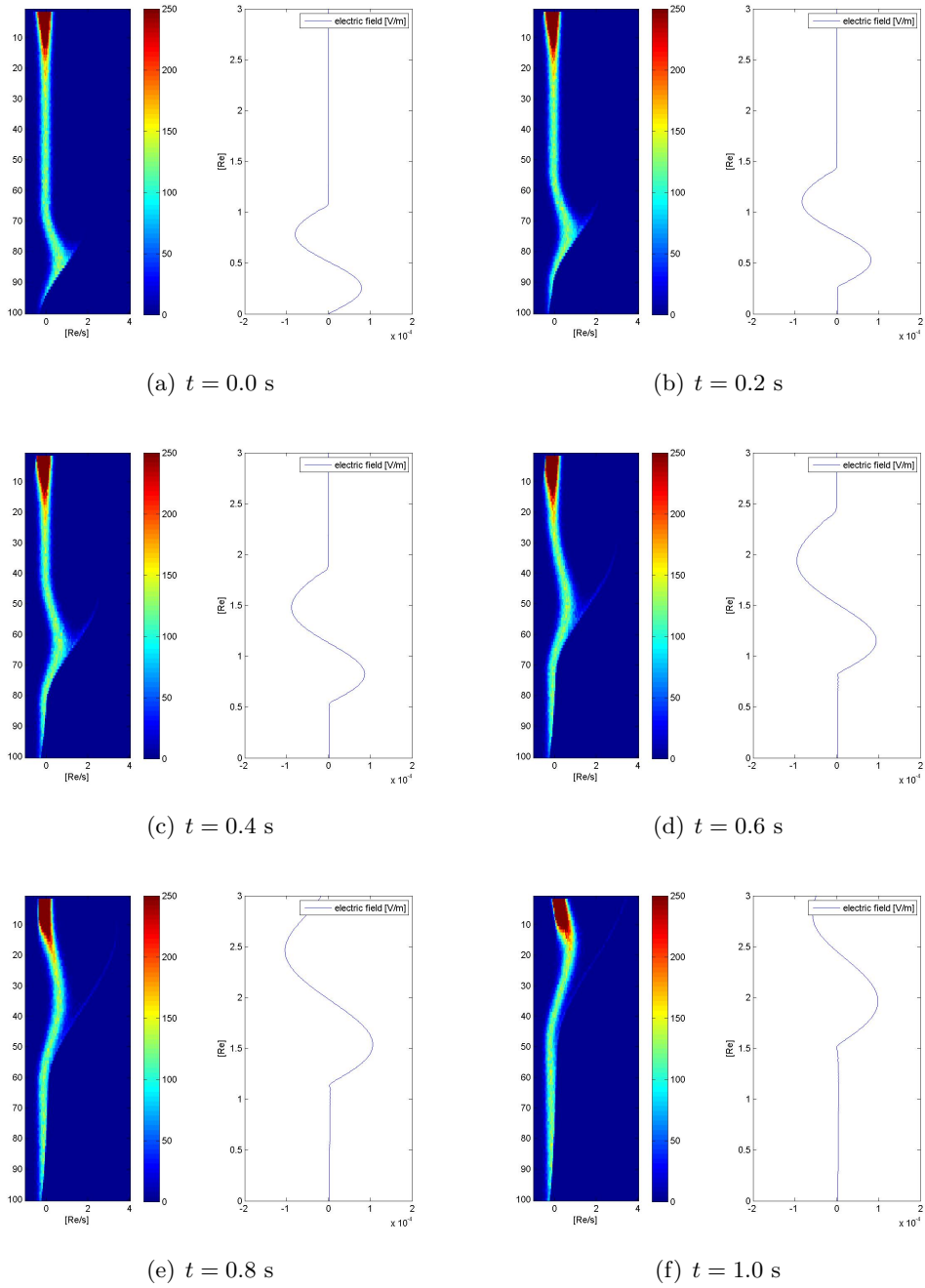


Figure 4.7: Wave propagation into an inhomogeneous magnetic field. The vertical axis represents distance along the magnetic field line $L = 4$, starting at the equator and going towards the ionosphere at higher latitudes. (*left*) Distributions of parallel velocities. Relative densities are constrained to values between 0 and 250. (*right*) Wave parallel electric field.

effect of a negative electric field, others under the influence of a positive electric field; it is evident that the gain (loss) of kinetic energy is proportional to the time a particle spends under the effect of a negative (positive) electric field, and the magnitude of the field.

The inhomogeneity in space of the background properties produce modifications on wave propagation, such changes were studied on section 3.3, where it was observed that the pulse increases (decreases) its amplitude, wavelength and phase speed as it moves to regions where the Alfvén speed is higher (lower). Nonuniformity on the background medium is also responsible for the magnetic mirror force pushing particles always towards the equator, and the force due to the electrostatic potential accelerating particles to higher latitudes. Despite all these effects, the most remarkable difference observed in figure 4.7 with respect to the homogeneous case (figure 3.4) is related to the wave. In the homogeneous case, it was observed an upper limit or maximum parallel velocity that a resonant particle would reach after interaction with the wave. In the inhomogeneous case, such limit is apparently removed, or at least it is set to a higher value.

This increase on the maximum velocity of resonant particles can be explained if the wave is propagating to regions of higher Alfvén velocity, which is the case here from the equator until somewhere after $2.5 R_e$ (see figure 4.2). As the propagation takes place, the pulse gets bigger in amplitude; the higher parallel electric field is capable of higher energization to electrons, which spend more time under its effect due to the increase of the wavelength. The wave phase speed is also increasing at this region; previously escaped particles could be trapped again by the wave and then accelerated again. These processes can take place over and over, and a fraction of the plasma will remain permanently in the acceleration region, gaining energy continuously and reaching very high parallel velocities, until the pulse reaches a region where the plasma density increases rapidly in space, lowering the Alfvén speed and consequently damping the wave.

4.4.1 Looking for unstable distributions

Mechanism of generation of the Horseshoe distribution

The way to explain the formation of a Horseshoe distribution involves the presence of both a converging magnetic field and an electric field directed antiparallel to the background magnetic field. Starting with a Maxwellian distribution in equilibrium, the electric field can accelerate electrons along the magnetic field. As the accelerated electrons move to regions of stronger magnetic field, the magnetic mirror

force produces deceleration in the parallel direction while increasing the velocity of gyration. Thus, this process should make particles migrate to higher parallel and perpendicular velocities, leaving the region of small velocities empty. The loss cone would also prevent the presence of reflected particles with small perpendicular velocities.

Observed distributions

To this point we have shown that there is enhanced parallel acceleration due to a wave pulse traveling to regions of higher Alfvén speed, with respect to propagation to regions of constant Alfvén speed. We are interested in knowing if this population of highly energized electrons can be a source for wave amplification via the ECM studied in section 1.2.3. In order for this to happen, we expect the distribution of accelerated electrons to present some positive gradient. More specifically, we expect the distribution take the shape of a *horseshoe* distribution sketched in figure 1.6.

Figure 4.8 shows the electron phase distribution in the neighbourhood of $s = 1.75 R_e$ at the moment the wave was influencing the local plasma. The phase diagram evidences parallel acceleration of virtually all the plasma, and a small component of resonant electrons with much higher parallel velocity component. The expected increase of the perpendicular velocity is not observed in the bulk plasma or in the resonant electrons. This suggests that the magnetic mirror force responsible of transferring moment from the parallel to the perpendicular direction is relatively small at that position; the electron cyclotron mechanism would perhaps take place at higher latitudes where the magnetic field lines converge faster. This remains to be investigated in the future.

Although the obtained results are by no means conclusive in explaining the existence of unstable distributions in the auroral cavity, these strongly suggest the realization of another simulation with a different parameterization of the ion density profile. The new parameters are to be chosen in such a way that the region where the Alfvén velocity profile grows is located where also the magnetic field is of much higher magnitude. This case is not studied here due to time constraints; at the time we are having these considerations, the program of studies for which this work is a requirement is at its end. Further studies including the case we just suggested are meant to be continued later.

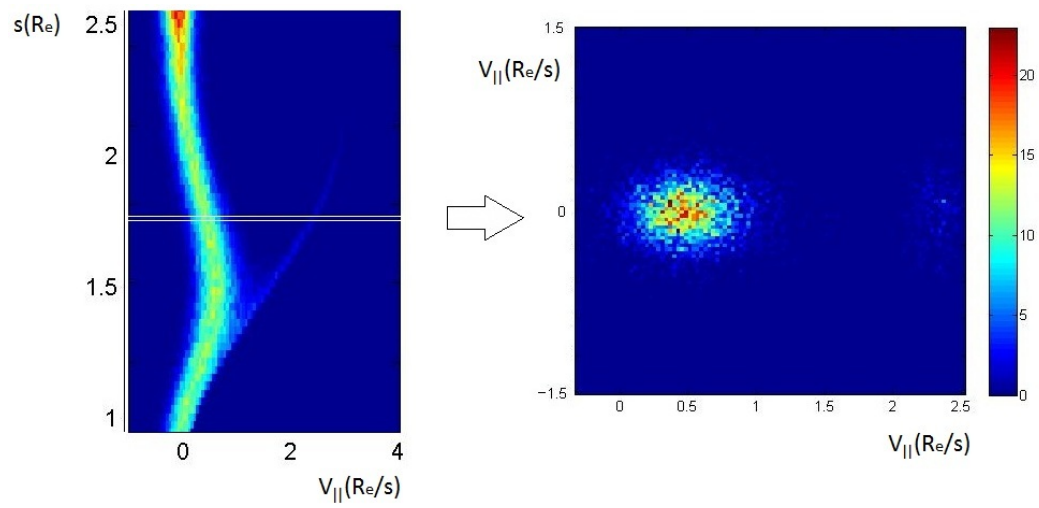


Figure 4.8: Local $(v_{\parallel}, v_{\perp})$ electron density at approximately $1.75 R_e$ at $t = 0.6$ s

Chapter 5

Conclusion

A computational code combining a test particle algorithm with a one dimensional wave propagation model has been written and tested to faithfully reproduce the physics of wave-particle interactions in plasmas whose properties resemble the conditions found in the auroral cavity, there is experimental evidence that points the auroral cavity as the source generator of AKR.

Chapter 2 provides a comprehensive introduction to the computational algorithm, which includes a derivation of the very basic aspects of particle movement and wave propagation characteristic of the high latitude, auroral region dominated by electron inertial effects. The model is intended to simulate the behaviour of electron distributions under the influence of inertial waves and background magnetic field, constant in time but nonuniform along the spatial domain. The wave scheme is valid for the case when the background particle density and magnetic field remain approximately constant in time. Particle motion is calculated under the assumption that the particles magnetic moment is constant and that velocity drifts due to the inhomogeneity of the magnetic field is negligible in the scale of time compared with the bouncing period of the wave.

The program start by defining background density and magnetic field profiles along the computational through analytic functions provided by the programmer. Different species of plasma, presumably in initial stationary state can be loaded independently by specifying some statistical parameters. Boundary conditions for particles can include the injection of particles of plasma at every interaction and the elimination of particles that naturally leave the space domain. Waves are incorporated gradually through one of the borders; a number of iterations at the beginning of the simulation are performed in order to incorporate the wave. Once the simulation starts, wave propagation is followed in time using an update scheme

that accounts for inertial effects. Trajectories of particles are calculated using a Runge Kutta 4 procedure that solves the motion equation including electric and magnetic forces. The electric field is the one associated with the wave, while the inhomogeneity of the magnetic field produces a magnetic mirror effect that tends to trap the particles. The resulting method accounts for wave particle interactions only, while particle-particle and particle-wave interactions are not considered.

Chapter 3 is devoted to report the results of several tests to the code itself, intended to confirm that it is capable of reproduce the physics of inertial Alfvén waves and particle movement in the presence of an external magnetic field. Tests have been implemented to measure the accuracy of the numerical scheme in the following aspects: 1. single particle dynamics, 2. wave propagation properties for ideal and nonideal numerical conditions in homogeneous media, 3. wave propagation properties in inhomogeneous media, 4. electron distribution evolution induced through conditions already published. The first two tests are compared to analytical predictions; measured differences are typically less than 1%. The fourth test presents also a very good agreement with other publications regarding electron acceleration through waves in homogeneous media.

Finally, chapter 4 reports the results of a simulation at which a wave pulse propagates into an inhomogeneous medium. Several theoretical considerations are taken into account in order to the initial distribution of particles to be loaded in its stationary state. Despite these considerations, the plasma loses its stationarity after a few hundred iterations. Nevertheless, a wave pulse was incorporated to the simulation. This pulse was sufficiently fast as to cross the whole spatial domain before the plasma changed significantly its original state. The resulting wave-plasma interaction revealed that higher levels of acceleration are possible in the inhomogeneous case. However, this simulation did not find the distribution of accelerated particles to be particularly unstable.

Concluding remarks and future work

Using our computational code, we have been able to look closely at the evolution of electron distributions under the effects of an inertial pulse traveling in an inhomogeneous space. The simulation reveals higher energization of the resonant electrons with respect to the homogeneous case due to the variation of the typical Alfvén velocity as the wave propagates, a condition which in principle favours a source of high energy available for the cyclotron maser. However, the obtained distributions present little instability in the perpendicular direction, a condition that has been pointed out to exist in the auroral cavity. It is suspected that the

magnetic force is relatively weak at the region where the wave is amplified due to the space inhomogeneity.

This first simulation strongly suggests a second try with different parameterization of the ion density profile. Modification of these parameters can be arranged such that the growing section of the Alfvén velocity profile is moved to a region where the magnetic field is stronger. Such case is not included here due to a time limitation of the program of studies for which this work is a requirement. Another way to complement this work would be to introduce a loss cone distribution as initial plasma instead of a Maxwellian, to determine how stationary behaves the plasma in this case.

Along with the few ideas suggested in the last paragraph, there is still plenty of work in which this code can be used. Tracing of particles was already used to help find out why the electrons did not have the expected distributions, some useful information was obtained, but a more careful analysis is still required and is not included here. Comparison of the results of this model with the ones from self-consistent models could be used to determine which features of the distribution dynamics are due to wave-particle interactions which are due to other kind of interactions. Finally, simulations with different λ_{\perp} dependence could be useful to characterize the *inertiality* of the plasma.

Bibliography

Baumjohann, W., and R. A. Treumann, *Basic Space Plasma Physics*, World Scientific, 1997.

Birdsall, C. K., and A. B. Langdon, *Plasma Physics via Computer Simulation*, Taylor & Francis Group, EE. UU., 2005.

Bittencourt, J. A., *Fundamentals of Plasma Physics*, 3 ed., Springer, 2005.

Box, G. E. P., and M. E. Muller, A note on the Generation of Random Normal Deviates., *Ann. Math. stat.*, 29, 610–611, 1958.

Chaston, C. C., C. W. Carlson, W. J. Peria, R. E. Ergun, and J. P. McFadden, FAST observations of inertial Alfvén waves in the dayside aurora, *grl*, 26, 647–650, 1999.

Chaston, C. C., C. W. Carlson, R. E. Ergun, and J. P. McFadden, Alfvén Waves, Density Cavities and Electron Acceleration Observed from the FAST Spacecraft, *Physica Scripta Volume T*, 84, 64–68, 2000.

Chaston, C. C., J. W. Bonnell, L. M. Peticolas, C. W. Carlson, J. P. McFadden, and R. E. Ergun, Driven Alfvén waves and electron acceleration: A FAST case study, *Geophysical Research Letters*, 29, 110,000–1, 2002.

Chu, K. R., The electron cyclotron maser, *Reviews of Modern Physics*, 76, 489–540, 2004.

Cramer, N. F., *The Physics of Alfvén Waves*, 1 ed., Taylor & Francis Group, 2001.

Ergun, R. E., C. W. Carlson, J. P. McFadden, F. S. Mozer, G. T. Delory, W. Peria, C. C. Chaston, M. Temerin, R. Elphic, R. Strangeway, R. Pfaff, C. A. Cattell, D. Klumpar, E. Shelly, W. Peterson, E. Moebius, and L. Kistler, FAST satellite

wave observations in the AKR source region, *Geophysical Research Letters*, *25*, 2061–2064, 1998.

Ergun, R. E., C. W. Carlson, J. P. McFadden, G. T. Delory, R. J. Strangeway, and P. L. Pritchett, Electron-Cyclotron Maser Driven by Charged-Particle Acceleration from Magnetic Field-aligned Electric Fields, *The Astrophysical Journal*, *538*, 456–466, 2000.

Ergun, R. E., L. Andersson, Y. Su, D. L. Newman, M. V. Goldman, W. Lotko, C. C. Chaston, and C. W. Carlson, Localized parallel electric fields associated with inertial Alfvén waves, *Physics of Plasmas*, *12*, 072,901–+, 2005.

Goertz, C. K., and R. W. Boswell, Magnetosphere-ionosphere coupling, *J. Geophys. Res.*, *84*, 7239–7246, 1979.

Hasegawa, A., and L. Chen, Kinetic processes in plasma heating by resonant mode conversion of Alfvén wave, *Physics of Fluids*, *19*, 1924–1934, 1976.

Kivelson, M., and C. Russell, *Introduction to Space Physics*, 1 ed., Cambridge University Press, Nueva York, 1995.

Kletzing, C. A., Electron acceleration by kinetic Alfvén waves, *J. Geophys. Res.*, *99*, 11,095–11,104, 1994.

Louarn, P., A. Roux, H. de Feraudy, D. L. Queau, and M. Andre, Trapped electrons as a free energy source for the auroral kilometric radiation, *J. Geophys. Res.*, *95*, 5983–5995, 1990.

Louarn, P., J. E. Wahlund, T. Chust, H. de Feraudy, A. Roux, B. Holback, P. O. Dovner, A. I. Eriksson, and G. Holmgren, Observation of kinetic Alfvén waves by the FREJA spacecraft, *Geophysical Research Letters*, *21*, 1847–1850, 1994.

Lysak, R. L., and C. W. Carlson, The effect of microscopic turbulence on magnetosphere-ionosphere coupling, *Geophysical Research Letters*, *8*, 269–272, 1981.

Melrose, D. B., Coherent Emission, *ArXiv e-prints*, 2009.

Melrose, D. B., and G. A. Dulk, Electron-cyclotron masers as the source of certain solar and stellar radio bursts, *The Astrophysical Journal*, *259*, 844–858, 1982.

Parks, G. K., *Physics of Space Plasma*, Westview Press, 2004.

- Paschmann, G., S. Haaland, and R. Treumann, *Auroral Plasma Physics*, Kluwer Academic Publishers, 2003.
- Pritchett, P. L., Relativistic dispersion and the generation of auroral kilometric radiation, *Geophysical Research Letters*, *11*, 143–146, 1984.
- Stasiewicz, K., P. Bellan, C. Chaston, C. Kletzing, R. Lysak, J. Maggs, O. Pokhotelov, C. Seyler, P. Shukla, L. Stenflo, A. Streltsov, and J. Wahlund, Small Scale Alfvénic Structure in the Aurora, *Space Science Reviews*, *92*, 423–533, 2000.
- Su, Y., R. E. Ergun, S. T. Jones, R. J. Strangeway, C. C. Chaston, S. E. Parker, and J. L. Horwitz, Generation of short-burst radiation through Alfvénic acceleration of auroral electrons, *Journal of Geophysical Research (Space Physics)*, *112*, 6209–+, 2007.
- Thompson, B. J., and R. L. Lysak, Electron acceleration by inertial Alfvén waves, *J. Geophys. Res.*, *101*, 5359–5370, 1996.
- Tikhonchuk, V. T., and R. Rankin, Parallel potential driven by a kinetic Alfvén wave on geomagnetic field lines, *Journal of Geophysical Research (Space Physics)*, *107*, 1104–+, 2002.
- Treumann, R. A., The electron-cyclotron maser for astrophysical application, *Astron. Astrophys. Rev.*, *13*, 229–315, 2006.
- Vogt, J., Alfvén wave coupling in the auroral current circuit, *Surveys in Geophysics*, *23*, 335–377, 2002.
- Watt, C. E. J., R. Rankin, and R. Marchand, Kinetic simulations of electron response to shear Alfvén waves in magnetospheric plasmas, *Physics of Plasmas*, *11*, 1277–1284, 2004.
- Wu, C. S., and L. C. Lee, A theory of the terrestrial kilometric radiation, *The Astrophysical Journal*, *230*, 621–626, 1979.